Titan's surface and atmosphere from Cassini/VIMS data with updated methane opacity

M. Hirtzig, B. Bézard, E. Lellouch, A. Coustenis, C. de Bergh, P. Drossart, A. Campargue, V. Boudon, Vladimir G. Tyuterev, P. Rannou, et al.

To cite this version:

M. Hirtzig, B. Bézard, E. Lellouch, A. Coustenis, C. de Bergh, et al.. Titan's surface and atmosphere from Cassini/VIMS data with updated methane opacity. Icarus, 2013, 226, pp.470-486. 10.1016/J.ICARUS.2013.05.033 . hal-00997595

HAL Id: hal-00997595
https://hal.science/hal-00997595

Submitted on 8 Mar 2023

HAL is a multi-disciplinary open access archive for the deposit and dissemination of scientific research documents, whether they are published or not. The documents may come from teaching and research institutions in France or abroad, or from public or private research centers.

L'archive ouverte pluridisciplinaire **HAL**, est destinée au dépôt et à la diffusion de documents scientifiques de niveau recherche, publiés ou non, émanant des établissements d'enseignement et de recherche français ou étrangers, des laboratoires publics ou privés.

Titan's surface and atmosphere from Cassini/VIMS data with updated methane opacity

M. Hirtzig[a, †], B. Bézard[a], E. Lellouch[a], A. Coustenis[a], C. de Bergh[a], P. Drossart[a], A. Campargue[b], V. Boudon[c], V. Tyuterev[d], P. Rannou[d], T. Cours[d], S. Kassi[b], A. Nikitin[e], D. Mondelain[b], S. Rodriguez[f], S. Le Mouélic[g]

[a] *Laboratoire d'Études Spatiales et d'Instrumentation en Astrophysique (LESIA), Observatoire de Paris - CNRS - UPMC - Univ. Paris Diderot, Meudon, France*

[b] *Université Grenoble 1/CNRS, UMR5588 LIPhy, Grenoble, F-38041, France*

[c] *Laboratoire Interdisciplinaire Carnot de Bourgogne, UMR 6303 CNRS-Université de Bourgogne, BP 47 870, F-21078 DIJON Cedex FRANCE*

[d] *Groupe de Spectrométrie Moléculaire et Atmosphérique (GSMA), Univ. de Reims-Champagne-Ardennes, Reims, France*

[e] *Laboratory of Theoretical Spectroscopy, Russian Academy of Sciences, Tomsk, Russian Federation*

[f] *Laboratoire AIM, Université Paris 7/CNRS/CEA, Centre de l'Orme des Merisiers, Gif/Yvette Cedex, France*

[g] *Laboratoire de Planétologie et Géodynamique de Nantes, CNRS UMR 6112, Univ. Nantes, France*

To be submitted to Icarus

Version 20 January 2013

[†] Presently at Fondation "La main à la pâte", Montrouge, France

ABSTRACT

We present an analysis of Cassini's Visual and Infrared Mapping Spectrometer (VIMS) data of Titan, making use of recent improvements in methane spectroscopic data in the region 1.3-5.2 µm. We first analyzed VIMS spectra covering a 8x10-km^2 area near the Huygens landing site in order to constrain the single scattering albedo (ω_0) of the aerosols over all of the VIMS spectral range. Our aerosol model agrees with that derived from Huygens Probe Descent Imager/Spectral Radiometer (DISR) in situ measurements below 1.6 µm. At longer wavelengths, ω_0 steadily decreases from 0.92 at 1.6 µm to about 0.70 at 2.5 µm and abruptly drops to about 0.50 near 2.6 µm, a spectral variation that differs from that of Khare et al.'s (1984) laboratory tholins. Our analysis shows that the far wings of the strong methane bands on both sides of the transparency windows provide a significant source of opacity in these windows, and that their unknown sub-Lorentzian behavior limits our ability to determine precisely the surface albedos. Below 1.6 µm, the retrieved surface albedos agree with those derived from Huygens/DISR. The VIMS spectrum at 2.0 µm indicates a surface albedo of 0.11±0.01, larger than derived in previous studies, and inconsistent with the signature of water ice. A series of VIMS data taken from 2004 to 2010 between 40°S and 40°N were then analyzed to monitor the latitudinal and temporal evolution of the atmospheric aerosol content. In the 2004-2008 period, the haze extinction is larger at Northern mid-latitudes by ~20% with respect to the Huygens site, whereas Southern mid-latitudes are depleted by ~15-20%. In 2009-2010, a progressive decline of the haze content in the Northern hemisphere is observed but no reversal of the North-to-South asymmetry is seen till mid-2010. Finally, data from five regions in Tui Regio and Fensal that show markedly different spectral behaviors and morphologies were analyzed to investigate the wavelength dependence of their surface albedo. The difference between bright and dark regions can be explained by different contents of small-sized tholins at the surface, brighter regions being more tholin-rich than dark regions, including the Huygens landing site. On the other hand, the albedo spectrum of the so-called "blue" regions, either dark or bright, can be explained by an excess of water ice particles, compared with the Huygens landing site. The spectrum of a 5-µm bright region in Tui Regio indicates a large excess of small-sized tholins relative to the Huygens site, but does not point to any particular surface composition.

1. Introduction

Titan, Saturn’s largest satellite explored by the Cassini-Huygens mission since 2004, is a complex world in which methane plays an important role. Information on the origin and evolution of the satellite relies on a good understanding of the origin and maintenance of methane in Titan’s atmosphere and the methanological cycle (Atreya et al. 2006) with all the processes and exchanges involved between the atmosphere, the surface and the interior it involves. In such studies, some information on these mechanisms is becoming available today, in particular by spectro-imaging techniques from the ground and space, but a meaningful analysis of these data demands a precise knowledge of the methane (CH_4) opacity on Titan.

Indeed, as Fink and Larson (1979) showed early on, Titan’s spectrum is dominated by aerosol absorption and methane scattering in the visible, and by methane absorption and aerosol scattering in the near infrared, where however, there exist several methane “windows” of weaker methane absorption; in combination with a decreasing with wavelength haze opacity, these windows permit the lower atmosphere and surface to be probed (McKay et al. 1989; Griffith et al. 1991). The haze extinction in the near-infrared region decreases with wavelength. Extracting information on the lower atmosphere and the surface of Titan from near-IR spectra thus requires a good understanding of the methane and haze contributions to the opacity.

Many attempts have been made to assess the absorption due to the isotopologues of methane. As detailed in de Bergh et al. (2012) and Campargue et al. (2012), three major approaches are applicable: direct laboratory measurements, theoretical calculations, and empirical models. Theoretical and experimental data were recently combined to cover the 0-8400 cm^{-1} (i.e. longward of 1.19 µm) range with a complete line-by-line description. The underlying spectroscopic information is based on a series of works on laboratory high-resolution experiments and theoretical analyses reported in Brown et al. (2003), Boudon et al. (2006), Albert et al (2009), Daumont et al (2013), Nikitin et al. (2002, 2006, 2013) below ~6000 cm-1 and in Wang et al. (2010a, b, 2010, 2011), Campargue et al. (2012) and Nikitin et al. (2011) at higher wavenumbers. The most recent spectroscopic results are the end-product of the CH4@TITAN project[2]. We used these data lists in a modular radiative transfer model capable of line-by-line as well as correlated-k calculations for planetary applications.

In this paper, expanding on the work initiated in de Bergh et al. (2012) and Campargue et al. (2012), we incorporate the new methane line list in a full-blown radiative transfer model to analyze a selection of Cassini/VIMS (Visible and Infrared Mapping Spectrometer) datacubes covering the seven methane windows available in the VIMS spectral range: 0.93, 1.08, 1.28, 1.58, 2.03, 2.69-2.79, and 5.0 μm. Our model thus represents an improvement with respect to the previous models, based on partial and/or older versions of the linelist (Bailey et al., 2011, Sromovsky et al., 2012; de Bergh et al. 2012; Griffith et al. 2012a,b).

We present here a two-fold analysis of VIMS data of Titan, focusing on Titan's lower atmosphere and then on its surface. We first constrain the single scattering albedo (ω_0) of the aerosols over the entire VIMS spectral range and determine the surface albedo spectrum at the Huygens landing site. We then monitor the evolution of the North-South Asymmetry (Lorenz et al. 1999; Hirtzig et al. 2006), characterized by different and varying populations of aerosol from one hemisphere to the other. Finally we extract surface spectra from several specific regions on Titan observed by VIMS, chosen for their variety of spectral responses, hinting at recent or past geological activity (Nelson et al. 2006; Solomonidou et al. 2012).

The use of Cassini/VIMS data allows us to benefit from a continuous spatial and temporal monitoring of the aerosol population and of the surface on Titan with good spatial resolution (~1-20 km/pixel) compared to Earth observations (~300 km spatial resolution at best), which we exploit here for a period of time of 6 years since the beginning of the Cassini mission.

2. Titan observations

The work presented here is based on the analysis of Cassini/VIMS spectra recorded over: i) the Huygens landing site, ii) the Tui Regio area (20°S, 135°W), and iii) the Fensal-Aztlan region (5°S, 50°W). We also analyzed spectra recorded from 2004 to 2010 in the northern and southern hemispheres and the equatorial region. The latter data were taken at low spatial resolution to monitor the large-scale aerosol distribution. The Cassini/VIMS hyperspectral datacubes used here are listed in Table 1, while Table 2 gives the observational characteristics (location, incidence and emission angle, phase…) for all the regions of interest (RoIs) we analyzed. On Fig. 1 the location of each RoI is indicated on the images of Titan's disk from the VIMS datacubes.

The Cassini VIMS consists of two camera instruments, a “pushbroom” mapping spectrometer that studies visible light (VIMS-VIS) and a “whiskbroom” mapping spectrometer for infrared light (VIMS-IR). VIMS “image cubes” contain information on 352 different wavelengths of light from ultraviolet to the mid-infrared. The visible channel produces multispectral images spanning the spectral range 0.3-1.05 μm over 96 spectral bands. The infrared channel covers the wavelength range 0.89-5.1 μm over 256 spectral bands. The spectral resolution (Full Width at Half Maximum, FWHM) is about 13 nm below 2.0 μm, increases up to 22 nm at 4.2 μm, and decreases to 18 nm at 4.8 μm. The calibration procedure of the infrared channel is described in McCord et al. (2006).

The signal-to-noise ratio (SNR) in the VIMS data was estimated from the observed pixel-to-pixel variability in a set of 3x3 spectra centered on the region of interest (RoI hereafter). To do so, we used the core of the methane bands, which are not sensitive to the surface albedo, and calculated the mean standard deviation of the intensity in the data set. We then interpolated the derived noise level between the methane bands. We did not use the windows as pixel-to-pixel variations may be caused by differences in surface composition or structure. We find that the SNR, per individual spectrum, typically reaches ~100 at short wavelengths, decreases to a few tens around 2-3 μm, and drops to unity longward of 4 μm.

Huygens Landing Site. In our previous tests (de Bergh et al. 2012), we used a VIMS spectrum of the Huygens Landing Site (HLS) extracted from the datacube CM 1477491859 and acquired during the first close Cassini flyby of Titan (tagged TA, October 26, 2004). For comparison, Griffith et al. (2012a) use three pixels from the CM 1481624349 datacube taken at TB (13th Dec 2004). The viewing geometry is very similar to the TA datacube (36°, 34°, and 18° incidence, emergence and phase angles compared to 33°, 28°, and 13° respectively), the major difference being the spatial resolution nearly twice better, reaching about 8 km/pix, and a much better Signal-to-Noise Ratio (SNR) due to a longer exposition time. Here we chose to consider a slightly different selection of pixels from this TB datacube than in Griffith et al. (2012a). Indeed, Fig. 1 of their paper show that the three pixels considered include (for two of them) large portions of the bright elevated cliffs observed by Huygens/DISR, while our selection of RoIs will focus mainly on dark terrains, like the one sampled by DISR inside the region interpreted as a dried riverbed. To follow the same notation as in Griffith et al. (2012a), we considered a weighted average of pixels [11, 3] (the one closest in coordinates to the HLS, and common to both studies), [11, 4], [12, 3], and [12, 4], with respective weights of 0.625, 0.125, 0.125, and 0.125. Note finally that the TA and TB VIMS spectra of the HLS show excellent consistency within error bars, so only the TB spectrum will be used.

Tui Regio and Fensal. Based on albedo and spectral classifications of the VIMS data, a distinction has been proposed between "dark" and "bright", and "blue" and "brown" regions (Barnes et al. 2005, Rodriguez et al. 2006, Soderblom et al. 2007a,b, Barnes et al. 2007, McCord et al. 2008, and references therein). Among the dark regions, "dark blue" have been tentatively proposed to consist of local enrichment in water ice (Rodriguez et al., 2006), while "dark brown" are often related to dune fields. Bright regions are also classified as "bright blue" or "bright brown" (Barnes et al. 2007). A particular class is some brightness-varying regions (and especially bright at 5-μm) spots; these regions have been claimed to be "active" (Nelson et al. 2006, 2009a,b), and perhaps related to cryovolcanism, although there remains significant controversy on the subject. Examples are Hotei Regio or Tui Regio. Here we analyzed VIMS spectra from the two datacubes used in Barnes et al. (2007), showing samples of the five types of regions. CM 1481619244 zooms over Tui Regio observed during TB and displays the three types of bright regions. CM 1514313117 is a close-up datacube on Fensal, taken during T9 and displaying the well-known "dark blue" and "dark brown" spectral units.

Large-scale aerosol distribution. We selected a series of 22 VIMS whole-disk images, taken over October 2004 – June 2010. Within each image, we selected three areas located around the Equator (index "E") and the northern ("N") and southern ("S") hemispheres. We chose as much as possible regions with incidence and emergence angles smaller than 60°. The three regions within a given VIMS cube were selected along the same meridian, varying from cube to cube, i.e. with no concern about the actual geographical location. This temporal study complements that of Rannou et al. (2010) who focused on the haze latitudinal structure, from detailed analyses of two VIMS observations: one targeted on the North polar region, obtained on (T22, 22 Dec 2006) and the other, acquired on (TA, 26 October 2004) and covering Titan's entire disk.

3. Radiative Transfer modeling

Our radiative transfer code is based on the plane-parallel version of the SHDOM (Spherical Harmonic Discrete Ordinate Method) solver (SHDOMPP; Evans 2007). The calculation may be either monochromatic (line-by-line) or spectrally integrated with a k-distribution of molecular opacity. The atmospheric model is described on a 70-layer grid extending from the surface up to 700 km (5×10^{-5} mbar). At each wavelength, the inputs to SHDOMPP are the layer optical depths, single scattering albedos and Legendre decomposition terms of the phase function. Up to 168 terms are used, and accordingly 168 streams to describe the radiation field. A Lambertian surface is assumed.

Opacity from aerosols and gases is taken into account. N_2-N_2 collision-induced absorption (CIA) coefficients are taken from McKay et al. (1989) and Lafferty et al. (1996) for the 2- and 4-μm regions respectively. Rayleigh scattering from N_2 and CH_4 is included (Peck and Khanna 1966, Weber 2003). Molecular line opacity due to methane and carbon monoxide is incorporated. The low resolving power of VIMS, reaching at most 300, justifies the use of correlated-k coefficients for each of the 256 infrared channels covering the 0.8-5.2 µm range. Four, eight or sixteen terms can be used to represent the CH_4 and CO opacity (16 were used here); they are pre-computed on a pressure-temperature grid defined from the HASI measurements (Fulchignoni et al. 2005). We used the methane vertical profile derived by Niemann et al. (2010) from Huygens/GCMS measurements and a uniform CO mole fraction equal to 4.5×10^{-5} based on Cassini/CIRS measurements (de Kok et al. 2009). D/H and $^{12}C/^{13}C$ isotopic ratios were set to 1.3×10^{-5} (Bézard et al. 2007) and 89×10^{-5} (Niemann et al. 2010) respectively. Note that fluorescence of CH_4 and CO, which is important at 3.3 and 4 µm respectively, is not modeled here.

3.1 Methane line parameters

Between 5854 and 7919 cm^{-1} (1.71-1.26 μm), we used the line list provided by Campargue et al. (2012). This line list was built in the framework of the CH4@TITAN project from spectra recorded at 296 and 80 K using Differential Absorption Spectroscopy (DAS) in the center of the tetradecad and isocad and high-sensitivity Cavity Ring Down Spectroscopy (CRDS) in the 1.58- and 1.28-μm transparency windows. It includes lines from the isotopologues $^{12}CH_4$, $^{13}CH_4$ and CH_3D. The variation of line intensity between the two temperatures provided the lower energy levels for most of the lines observed at 80 K. For the other ones, we set the lower energy level to 100 cm^{-1}.

For the region below 5854 cm^{-1} (above 1.71 μm), we calculated the CH_4 line parameters for the pentad, octad and tetradecad, from a global analysis as described in Albert et al. (2009)

and Boudon et al. (2006). The octad range has been recently improved by Daumont et al. (2013). These analyses are based on an expansion of the effective Hamiltonian to high order, using a set of high-resolution rovibrational spectra. We then obtained a set of $^{12}CH_4$ lines up to 6757 cm^{-1} (1.48 μm) and $^{13}CH_4$ lines up to 3501 cm^{-1} (2.86 μm).

In a given spectral interval, the bands of CH_3D correspond to higher vibrational excitations because of the isotopic shifts. The intensity measurements and analyses for line intensities of this isotopologue are thus less advanced than for $^{12}CH_4$. Here we used a CH_3D linelist which is a compilation from various analyses and extrapolations, mostly based on the works by Nikitin et al. (2002, 2006) below 3700 cm^{-1} and Nikitin et al (2013) in the 4000-4550 cm^{-1} range. The contribution of weak bands in the range 3700-4000 cm^{-1} is not important for this study. The range 4500-5000 cm^{-1} is based on preliminary calculations in progress; the opacity could be somewhat underestimated at the higher wavenumber edge because of missing measurements.

These line parameters were used to calculate k-correlated coefficients for the VIMS infrared channels between 1.2797 and 5.1254 μm. No complete line list is available at wavenumbers above 7919 cm^{-1} (below 1.263 μm). For VIMS channels below 1.2797 μm, we used the methane absorption coefficients derived by Karkoschka & Tomasko (2010) from Huygens/DISR in situ measurements of methane absorption during the descent to Titan's surface. The measurements were performed by the Upward Looking Visible Spectrometer (ULVS) in the range 0.52-0.96 μm at a resolution of ~5 nm and by the Upward Looking Infrared Spectrometer (ULIS) in the range 0.88-1.6 μm at a resolution of ~20 nm. A constant value of -0.016 km^{-1} amagat^{-1} was added to the ULIS-derived coefficients as justified in Campargue et al. (2012). We also tested the absorption coefficients derived by Tomasko et al. (2008a) using ULIS measurements having the Sun in the field of view during most of the data collection time (see Section 4.3.5). In this case, a constant coefficient of 0.024 km^{-1} amagat^{-1} was added to the listed coefficients, following Campargue et al. (2012).

In some cases we also tested the band model constructed by Karkoschka and Tomasko (2010) from a combination of DISR-derived absorption coefficients with laboratory measurements and HST observations of Jupiter. The k-correlated coefficients were generated from this band model using a method similar to the one described in Irwin et al. (2006).

The Lorentz halfwidth was fixed to 0.065 $(T_0/T)^{0.85}$ cm^{-1} atm^{-1} (T_0=296 K), based on laboratory measurements by Lyulin et al. (2012) in the 1.7-μm band. We initially used the same sub-lorentzian χ factor as in Campargue et al. (2012):

$$\chi = 1 \text{ for } \Delta\sigma \leq 25.6 \text{ cm}^{-1},$$

$$\chi = 1.2378 \exp(-\Delta\sigma/120.0) \text{ for } \Delta\sigma > 25.6 \text{ cm}^{-1},$$

where $\Delta\sigma$ is the distance from line center (cm^{-1}). This line profile allowed Campargue et al. (2012) to reproduce correctly the low-frequency wing of the 1.58-μm window in Titan's spectra. As shown in the following Section, we tested other χ factors at longer wavelengths.

3.2 Aerosol model

Analyzing a large set of Huygens/DISR data, Tomasko et al. (2008b) proposed an aerosol model in terms of number density, extinction, phase function and single scattering albedo (w_0) as a function of altitude between 0.35 and 1.6 μm. De Bergh et al. (2012) showed that this aerosol model does not allow us to reproduce the VIMS observations near the Huygens site (10.3°S, 192.3°W) between 1.4 and 1.7 μm. A large fraction of the disagreement is due to the addition by Tomasko et al. (2008b) of a backscattering peak in the phase function below 80 km, which they did not justify longward of 0.934 μm. De Bergh et al. then chose to use the same phase function below and above 80 km. We did the same here, and used the values in Table 1a (phase function above 80 km) of Tomasko et al. (2008b) to calculate the Legendre coefficients at all atmospheric levels from 0.8 to 5.2 μm.

As a nominal case, we used the optical depth profiles of Tomasko et al. (2008b, their Table 3) both above 80 km ("haze" region) and below 80 km ("mist" regions : 0-30 km and 30-80 km). As a free parameter, we only allowed for a single uniform multiplying factor to account for horizontal variations of aerosol opacity. As detailed in Section 4, we determined the single scattering albedos by fitting the I/F reflectivity measured by VIMS in the core and the wings of the methane bands near the Huygens landing site. Up to 1.28 μm, we allowed for different values of w_0 in the haze and in the mist regions and actually used the values of Tomasko et al. (2008b, their Table 2, Cols. 2-3). Beyond 1.28 μm, a single value of w_0 is used in both altitude regions. In conclusion, once w_0 is determined from VIMS data near the Huygens landing site, the only free parameter of the haze model is a uniform scaling factor for the number density, or accordingly the integrated optical depth.

3.3 Method and error estimation

To retrieve the surface albedo from the VIMS data at a given location, we first derived the haze optical depth from the I/F reflectivity in the methane bands. This was done by minimizing the residuals between observations and calculations over spectral intervals that include the core and near wings of each methane band. This haze scaling factor, relative to the Tomasko et al. (2008b) model, bears a typical uncertainty of ± 0.05. With this best fit model, we produced two simulations with constant 0.05 and 0.5 surface albedos and assumed that the outgoing intensity varies linearly with surface albedo between these two values. We checked this assumption for various test cases and found that the variation is almost exactly linear longward of 2.1 μm while this assumption induces an error of at most 3% on the retrieved surface albedo, near 0.9 μm.

We also took into account the uncertainty on the surface albedo due to noise level. As discussed in Section 2, the signal-to-noise ratio (SNR) in an individual spectrum varies from ~100 in the short-wavelength windows to ~1 longward of 4 μm. The error induced is taken as the variation of the surface albedo that yields a relative 1/SNR variation of the I/F reflectivity.

The uncertainty on the haze extinction introduces a significant uncertainty on the retrieved surface albedo. To illustrate this, we considered the VIMS spectrum of the Huygens landing site recorded during Flyby TA, which was also used in de Bergh et al. (2012). The value we inferred for the haze scaling factor is 1.03, not too far from the 0.90 factor derived by de Bergh et al. (2012). Table 3 shows the uncertainty on the retrieved surface albedo due to the 5% uncertainty on the haze extinction. As expected, the error bars are larger in the wings of the methane windows (e.g. at 1.54 μm) than in the centers (e.g. at 1.59 μm), as we lose sensitivity to the surface. We also note that the uncertainty varies from one window's center to another due to different transparencies (gas and aerosols). The 0.93- and 1.08-μm windows are the least transparent, while on the contrary the 2.03-μm window is so transparent that changing the aerosols has little impact on the retrieved surface albedo. In any event, the maximum total error on the retrieved albedos at the peak of the windows is ± 19%. These uncertainties, derived from a specific case, are considered as applicable to all of the VIMS spectra considered here.

Calibration uncertainties of the VIMS datacubes, which are not very well documented, have not been taken into account. In the fitting procedure, we considered error bars due to random noise, to the aerosol model, as discussed above, and to systematic uncertainties in the representation of the model opacity (mainly due to unknowns in the far wing lineshape).

4. Analysis of VIMS spectra of the Huygens landing site and atmospheric model

We begin with an analysis of a VIMS spectrum including the Huygens landing site ("HLS" from now on). The higher spatial resolution DISR observations of the same region have permitted to retrieve aerosol properties (number density, extinction, phase function and single scattering albedo (w_0) over 0.6-1.6 μm) as a function of altitude (Tomasko et al. 2008b), but these results relied in part on the adopted description of the methane absorption properties. With the line-by-line information on the CH_4 that is now available longward of 1.26 μm, we first test the aerosol model of Tomasko et al. (2008b) against the VIMS spectrum of the HLS. We then use the VIMS spectral coverage to extend the aerosol model over a broader range, and to investigate the role of far-wing absorption properties of CH_4 in the windows opacity. The so-defined atmospheric model will be used in sequence for monitoring the aerosol distribution through time (Section 5) and for the analysis of other regions of interest (RoIs) in Section 6.

4.1 Testing aerosol models from the 1.27-1.70 μm range

Fig. 2 shows the 1.27-1.70 μm range of VIMS spectrum constructed in this manner, compared with several models. Focusing first on fitting of methane bands and wings Fig. 2 shows that the nominal aerosols model by DISR (Tomasko et al. 2008b) produces a poor fit (blue line) of the data, in particular in the 1.4 μm band: the core of the band is under-estimated, while the wings are quickly over-estimated. We attempted to improve the fit by keeping the DISR extinction profile ("100 % DISR") but changing the single scattering albedo of the aerosols to 1.00 in the stratosphere and 0.95 in the troposphere. Although this modification (green line in Fig. 2) does slightly increase the flux in the core of the 1.4 μm band the improvement is minor, and the reflectance remains over-estimated at 1.45-1.54 μm. Furthermore, this leads to an unsatisfactory situation in which aerosols are brighter in the stratosphere than in the troposphere, a behavior opposite to inferences from DISR measurements. We thus adopted an alternative approach, i.e. considered a mono-modal (i.e. haze = mist) regime, in which the single scattering albedo values (ω_0) found for the stratosphere by DISR – and decreasing from 0.94 at 1.28 μm to 0.92 at 1.58 μm – are taken as constant as a function of altitude. As is clear from Fig. 2 (red line) this choice permits a good fit of the 1.45-1.54 μm wings although the problem remains in the band core. Griffith et al. (2012a) found the same problem, and also decided to emphasize the fit of the wings. The quality of the fit we obtained is similar to that of de Bergh et al. (2012) who used a scattering albedo larger than ours by 0.02 below 80 km but reduced the optical depths of Tomasko et al. (2008b) by 10%.

4.2. Determination of the aerosol single scattering albedo over 0.95-5.1 µm

Proceeding with this approach, and still keeping 100 % of the DISR opacity, Fig. 3 (top panel) shows the comparison of the entire VIMS spectrum over 0.9-5.1 μm with a series of models in which the haze/mist single scattering albedo is varied over 0.50-1.00 by steps of 0.10. In this plot, only regions corresponding to band cores and band wings are shown, since windows are also sensitive to surface albedo. In the middle panel of Fig. 3, a single scattering albedo "spectrum" is inverted (grey points with error bars) so that the associated model exactly matches the VIMS spectrum, whenever possible. This "spectrum" is compared to calculations of ω_0 using the optical constants of Khare et al. (1984) modified by Rannou et al. (2010, Fig. 14), assuming fractal particles made of 3000 0.05 μm radius monomers (Tomasko et al. 2008b). Although both the spectrum inferred from VIMS and the calculations based on Khare et al. (1984) agree on a general decrease of the single scattering albedo with wavelength, the match is not particularly good; notably the VIMS-inferred ω_0 spectrum decreases more steadily over 1.5-2.5 μm. Longward of 3 μm, results are more uncertain, due to the difficulty to fit the observed VIMS spectrum in regions of low I/F.

As indicated above, the top panel of Fig. 3 assumes unmodified DISR opacities. In an attempt to better constrain the spectral behavior of ω_0, the bottom panel of Fig. 3 shows the simultaneous effect of the single-scattering albedo and of the aerosol opacity, expressed as a haze scaling factor (F) from the DISR reference. Results are expressed in the form of contours of reduced χ^2 (i.e. χ^2 divided by the number of points) in the (ω_0, F) domain, where the fit is applied to a series of six regions of strong methane absorption around 1.14, 1.40, 1.70, 2.40, 3.10 and 3.60 µm. The contours of equal χ^2 form valleys indicating a partial correlation of ω_0 and F; this can be expected as to first order brighter aerosols have the same effect as a larger extinction. Furthermore all six spectral regions are consistent with the 100 % DISR extinction case (F=1) providing χ^2 close to the minimum, and the best solutions for ω_0 in the first three bands (1.14, 1.40, 1.70 µm) are very similar to those inferred from DISR. This justifies that we select F = 1 and spectrally adjust the single scattering albedo.

Nonetheless, as discussed previously in the case of the 1.4-μm band, it is difficult to reproduce methane bands and wings simultaneously, and the fitting approach based on the last panel of Fig. 3 gives over weight to band cores (as do the grey points in the middle panel). Rather, and especially in view of deriving surface albedos, we consider more important to match line wings as closely as possible, even at the expense of imperfect fitting of the regions of strong absorption. Fig. 3 (bottom panel) still provides some guidance on the choice of sensible values of ω_0 while keeping 100% DISR extinction. Longward of 3 μm, the SNR is so low (and progressively limited by digitization noise) that χ^2 contours have little value, so that based on the 3.10 μm results, we adopt $\omega_0 = 0.5 \pm 0.1$.

The red line in the middle panel of Fig. 3 is the single scattering albedo dependence we finally adopted. Note that below 1.28 μm, we strictly retain the DISR results with a bimodal description of the aerosols and the associated single scattering albedos (shown as the red (mist) and yellow (haze) diamonds). Only above 1.28 μm do we switch to a mono-modal description. Between 1.28-1.58 μm, the ω_0 follow the DISR-derived stratospheric values (i.e. 0.94 and 0.92 at the two wavelengths, respectively).

4.3. Atmospheric model and surface albedo in the methane windows

In this Section, we fit the spectrum in all the methane windows to constrain the surface albedo, using the adopted aerosol model. In this process, we are led to fine-tune the CH_4 models, i.e. determine suitable far-wing line profiles.

4.3.1. The 1.1-1.8 µm range

The 1.1-1.8 μm range is only partly covered by our line list, which stops at 7919 cm^{-1} (1.263 μm). As indicated in Section 3, line parameters were used to calculate k-correlated coefficients for the VIMS channels at 1.2797 μm and above. Below 1.2797 μm, we used the methane absorption coefficients derived by Karkoschka & Tomasko (2010) from DISR/ULIS measurements (their Table 3), corrected by -0.016 km^{-1} amagat^{-1}, as found appropriate for the 1.28 μm window by Campargue et al. (2012).

Fig. 4 (left panel) shows the fit of the 1.1-1.8 μm range of the VIMS TB spectrum of the HLS using the previous aerosol model (Section 4.2) and various values of the surface albedo. As indicated before, the far wing profiles were described using the same sub-Lorentzian factor as in Campargue et al. (2012). We find that the surface albedo providing the best fit at 1.28 μm is ~0.155 decreasing to ~0.08 at 1.52-1.56 μm and re-increasing to ~0.10 at 1.58 μm. These values are entirely compatible with the surface albedo derived from DISR spectra (Jacquemart et al. 2008) in these windows. This conclusion is confirmed in the right panel of Fig. 4, which shows fits for multiplicative factors (0.8, 1, and 1.2) of the Jacquemart et al. (2008) albedo spectrum. As indicated in Section 3.3, error bars on the best fit surface albedos are due not only from S/N limitations (typically +/-0.01 in surface albedo), but also to errors due to uncertainties on the haze model. These haze uncertainties, typically 5 % on the extinction, induce +/-4 % and +/- 6 % errors on the 1.28 and 1.58 μm surface albedos, but a much larger value (+/- 34 %) at the less transparent 1.54 μm wavelength (Table 3).

4.3.2. The 2 µm window

As the influence of aerosols steadily decreases with wavelength, the 2-μm window shows enhanced sensitivity to the surface as shown in Table 3. To model this window, we considered both the Karkoschka and Tomasko (2010) band model (their Table S1, hereafter “K&T”), and the k-correlated coefficients calculated from our line list (see Section 3, hereafter “line list”). In the latter approach, we tested the effect of different descriptions of the far wing absorption, i.e. sub-Lorentzian factors decreasing as $\exp(-\Delta\sigma/158)$ or $\exp(-\Delta\sigma/200)$ beyond 26 cm^{-1} from line center, where $\Delta\sigma$ is the line distance in cm^{-1}. This parameter is important as the red wing of the-2 μm window is strongly sensitive to the far wings of the very strong CH_4 lines at 2.3-2.4 μm.

The simulations shown in the first panel of Fig. 5, performed with a constant surface albedo of 0.11, illustrate that the K&T (brown) and line list (blue, red) models do not predict the same spectral shape for the 2-μm region. In fact using the “K&T” coefficients produces a window peak shifted by about 0.02 μm compared to observations. Fitting the observed spectral shape with these methane coefficients would require forcing a steep decrease of the surface albedo within the window, from ~0.17 to ~0.06 over 2.05-2.10 μm. In contrast, using the "line list" coefficients permits to fit the window shape with an essentially constant surface albedo. This is true in particular with an $\exp(-\Delta\sigma/200)$ dependence of the χ-factor (beyond 26 cm^{-1} from line center) for which the fit with a constant 0.11 surface albedo is excellent. The second panel of Fig. 5 shows the sensitivity of the spectrum to the surface albedo for this model. Considering the effect of noise and of the uncertainty on the methane far wing profiles, we infer an albedo of 0.11±0.01. Note (Table 3) that haze uncertainties have a negligible effect on surface albedo in this window and at longer wavelengths.

We also tested the line wing description adopted by Griffith et al. (2012), i.e. an abrupt absorption cut-off of the Voigt profile at 500 cm^{-1} from line center, instead of a χ-like dampening function. This case (green line in the first panel of Fig. 5) not only would require a larger surface albedo to match the peak I/F, but also produces a shoulder near 2.1 μm that is not visible in the data.

Griffith et al. (2012) find a 2 μm surface albedo of ~0.05, less than half our value. In part, this is because they used aerosol optical properties of Khare et al. (1984), which are much brighter than ours at 2 μm, thus limiting the need for a bright surface albedo. The effect of the single scattering albedo (ω_0 = 0.98 vs 0.76) is shown in the last panel of Fig. 5, assuming again an $\exp(-\Delta\sigma/200)$ dependence for the χ factor. A single scattering albedo of ~0.76 is then required to fit the regions 1.85-195 and 2.1-2.2 μm which are not sensitive to surface albedo. On the other hand, we found that, using ω_0 = 0.98 in combination with a 500 cm^{-1} cut-off allows us to recover a satisfactory fit of the window (not shown in Fig. 5). Hence the discrepancy between our findings and Griffith et al. (2012) at 2 μm can be attributed to the combined effect of different assumed haze optical properties and different adopted line wing properties.

Finally, we note that for all the models based on our line list, the secondary I/F peak near 1.9 μm is greatly overestimated. In contrast, this peak is correctly reproduced with the Karkoschka & Tomasko (2010) model. The missing absorption in the line list model may be a missing CH_3D signature, since we included CH_3D bands only above 2.17 μm. CH_3D spectra recorded in Zurich and reported by Ulenikov et al. (2010) do show significant absorption in the interval 1.86 – 1.94 μm.

4.3.3. *The 2.4-3.2 µm range*

The 2.4-3.2 µm range includes a 2.7 µm window exhibiting a complex, double peak structure, with peaks at 2.69 and 2.79 µm (Fig. 6). As Griffith et al. (2012) showed (their Fig. 6), this region is sensitive to the (probably spectrally-dependent) single scattering albedo (ω_0) of the haze, the surface albedo, the small but significant features of CH_3D in the 2.6-3.0 µm range, and the far wing profile of the CH_4 pentad lines around 3.3 µm, which may hide or not the isotopologue's signatures. We only show here calculations based on our CH_4 and CH_3D line list (Section 3).

Similarly to Fig. 6 of Griffith et al. (2012), Fig. 6 illustrates the effect of: (top panel, left side) methane far wings; (bottom panel) aerosol ω_0 spectrum; (top panel, right side) the surface albedo. For this, we consider a nominal model, having (i) a $\exp(-\Delta\sigma/120)$ dependence of the χ-factor beyond 26 cm^{-1} from line center (ii) the ω_0 spectrum shown in Fig. 3 (iii) a surface albedo of 0.03. This nominal model is shown in black lines in all panels of Fig. 6. One parameter at a time is then varied, the others being fixed at their nominal values.

As is clear in the top left panel of Fig. 6, far wings of the strong CH_4 pentad lines that absorb too much will dominate over the CH_3D lines at 2.7-2.8 µm, tending to erase the structure of the 2.7-3.0 µm region, as occurs with an $\exp(-\Delta\sigma/158)$ profile (green line). A stronger dampening (the nominal $\chi = \exp(-\Delta\sigma/120)$ case, black line) better preserves the features of the window. However, for this model and spectrally constant surface albedo, the 2.79 µm peak is slightly darker than the 2.69 µm one, whereas observations reveal that it is significantly brighter. We tried to solve this shortcoming by limiting even more the influence of the strong pentad lines; for this we considered a hybrid far wing profile, starting as $\exp(-\Delta\sigma/120)$ beyond 26 cm^{-1} from line center, then dropping as $\exp(-\Delta\sigma/60)$ beyond 200 cm^{-1}. This simulation, in red, indeed allows the 2.79 µm window to be the brightest again, but a new window appears at 2.92 µm (sensitive to the surface), in contradiction with the observations. As a result, for the pentad lines we retained the $\exp(-\Delta\sigma/120)$ χ profile.

The bottom panel of Fig. 6 explores the influence of the aerosol single scattering albedo. Here constant ω_0 values of 0.5 and 0.8 are considered (green and red lines), as well as the Khare-derived (light blue line) and nominal ω_0 (black line) spectra, both of which are shown in Fig. 3. A ω_0 value of 0.8 is needed to reproduce the shape of the 2.4-2.6 µm region, while $\omega_0 \sim 0.5$ is well suited to the 2.8-3.2 µm range. While a transition between these two regimes can be expected based on the general Titan aerosol properties, it is rather difficult to characterize it spectrally. Based on the (modified) Khare et al. (1984) coefficients from Rannou et al. (2010), one can expect a rather sharp drop of single scattering albedo in the 2.7-3.0 μm range from 0.9 to 0.3, with the inflexion point (maximum slope) around 2.8 μm. In our preferred model, the drop is smaller in amplitude (albeit even more abrupt), decreasing from 0.7 at 2.61 μm to 0.55 at 2.65 μm, and 0.46 by 2.8 μm; the point of maximum slope is shifted by about -0.1 μm compared to the model based on Khare et al. (1984). Griffith et al. (2012) find a single scattering albedo of 0.63+/-0.05 at 2.64-2.82 μm, comparable to our values and also below expectations for Khare-like tholins.

For the nominal haze model and far-wing model, varying the surface albedo (top right panel of Fig. 6) indicates that matching the 2.69 and 2.79 μm peaks requires surface albedos A_s = 0.05 and 0.07 respectively, while fitting the flux level between the two would imply A_s = 0.03 there. Given the difficulties associated with the 2.7-μm window, we need to be cautious about these spectral variations. We rather consider them as independent measurements of the same quantity, concluding that A_s = 0.05+/-0.02 at 2.7 μm. We also note that fitting the two peaks with the same surface albedo could be achieved by increasing artificially the haze single scattering albedo by ~0.1 from 2.69 to 2.79 μm, but we do not regard this as physically plausible.

4.3.4. The 5-µm window

The 5-μm window in VIMS observations is noisier than the other windows (SNR~1 per individual spectrum). As indicated in Section 3, we modeled this window using k-correlated coefficients generated from our methane line list. Methane opacity at 5 μm actually results from far wings of the strong ν_4 band at 7.7 μm for which we nominally assumed a χ factor varying as $\exp(-\Delta\sigma/120)$, but also tested a $\exp(-\Delta\sigma/158)$ dependence. The 5-μm window is limited on its blue wing by CO absorption in the (1-0) band centered at 4.7 μm, and as demonstrated by Lellouch et al. (2003), model results are sensitive to CO line wings. We here assumed for CO a χ factor equal to $\exp(-\Delta\sigma/50)$, a simple and reasonably accurate approximation of the more precise Brodbeck et al. (1994) far wing profile used by Lellouch et al. (2003). Fig. 7 indicates that our models overestimate the absorption at 4.85-4.95 μm. This is consistent with the fact that (i) we assumed a uniform CO mixing ratio of 45 ppm, while Lellouch et al. (2003) found that a 32 ppm mixing ratio was providing an adequate fit to their (high-resolution) spectrum (ii) we included CH_4 absorption, omitted by the authors; the fact that methane absorption is actually not negligible is illustrated in Fig. 7. Our model does not include fluorescent CO emission (Lòpez-Valverde et al. 2005), which is responsible for the very low emission level (I/F ~0.002-0.01 over 4.5-4.8 μm) that appears quasi-continuum like at VIMS spectral resolution. None of these limitations is prohibitive since our goal here is merely to determine the surface albedo, primarily determined from the I/F at 5.0 μm. Accounting for the low S/N (largely limited by digitization noise) and for the uncertainty on the far-wing profile, we conclude on a surface albedo of 0.03±0.01 at the HLS (Fig. 7). The TB spectrum would further suggest an albedo drop over 5.0 – 5.1 μm, but such a behavior is not confirmed in the TA spectrum.

4.3.5. *The 0.9-1.2 µm range*

Two windows are present in this range, centered at 0.94 and 1.08 μm (Fig. 8). The VIMS spectral resolution limits the number of useful data points, with only 1 and 2 channels, respectively, probing the surface. As line-by-line information is not available for methane at wavelengths shorter than the 1.28-μm window, one must rely on band models. As in Campargue et al. (2012) for the 1.28-1.6 μm range, we tested two methane transmission models derived from DISR measurements within Titan’s atmosphere. We used (i) the Tomasko et al. (2008a) coefficients (their Table 4), deduced from DISR/ULIS (880-1600 nm) measurements and (ii) the DISR-derived coefficients from Karkoschka and Tomasko (2010), using DISR/ULVS values at 520-960 nm (their Table 2) and DISR/ULIS values at 960-1600 nm (their Table 3). Note that the ULVS and ULIS sub-instruments have different spectral resolutions (5 and 20 nm, respectively). In the DISR/ULIS range, one difference between the analysis of Tomasko et al. (2008a) and Karkoschka and Tomasko (2010) is that the former authors assumed zero absorption at 1.289 μm while the latter assumed a 0.04+0.02/-0.01 km^{-1}amagat^{-1} absorption. In the 1.28-1.6 μm range Campargue et al. (2012) found that corrections by +0.024 km^{-1}-am^{-1} and -0.016 km^{-1}-am^{-1} to the two sets of coefficients, respectively, are needed to bring them (especially those of Tomasko et al. 2008a) in agreement with line-by-line calculations using the WKMC database. Finally, we also tested (as case iii) the band model constructed by Karkoschka and Tomasko (2010) from a combination of DISR-derived absorption coefficients, laboratory measurements and HST observations of Jupiter (their Table S1).

Fig. 8 (left panel) shows our modeling of the 0.90-1.20 μm range, using the unmodified DISR aerosol model (i.e. keeping the bimodal haze/mist distribution, and 100 % of the haze opacity). Calculations are performed using (i) the Tomasko et al. (2008a) coefficients shifted by +0.024 km^{-1} amagat^{-1} at all wavelengths (ii) the composite ULIS/ULVS coefficients from Karkoschka and Tomasko (2010), corrected by -0.016 km^{-1} amagat^{-1} longward of 1 μm and (iii) the band model from Karkoschka and Tomasko (2010). All calculations were done using a surface albedo of 0.17. Note that the calculations were here performed with the CH_4 vertical profile of Niemann et al. (2005), to maintain consistency with the Tomasko et al. (2008a) and Karkoschka & Tomasko (2010) analyses.

Fig. 8 shows that the band model of Karkoschka & Tomasko (2010) does not permit a good match of the 1.08-μm window, as it significantly overestimates its blue wing over 1.03-1.06 μm. In contrast, when the -0.016 km^{-1}-am^{-1} correction is applied to the ULIS coefficients, the ULVS/ULIS coefficients permit a good fit of the line wings. With this model, a reasonable fit of the entire 0.90-1.20 μm range is obtained for a surface albedo of 0.17 – consistent with Jacquemart et al. (2008). Note however that (i) the two VIMS channels probing the 1.08-μm window (i.e. 1.065 and 1.083 μm) would suggest slightly higher and smaller albedos, respectively, and that (ii) the model slightly over-predicts the 0.94-μm window, whose weak dependence on surface albedo therefore implies a significantly lower best fit surface albedo. Using the modified Tomasko et al. (2008a) extinctions along with the same surface albedo of 0.17 also permits to match the 1.08-μm window, but the 0.94-μm window is strongly under-predicted. This is no surprise, as the Tomasko et al. (2008a) coefficients were derived from ULIS data at a resolution of 20 nm, significantly coarser than VIMS (13 nm). We conclude here that the Karkoschka & Tomasko (2010) ULVS/ULIS absorption coefficients, modified as per the recommendation of Campargue et al. (2012), provide the best available description of the methane opacity in this region, and we infer best fit surface albedos of 0.135 at 0.94 μm and 0.16 at 1.08 μm. Including error bars due to haze (Table 3) in these less transparent windows, the uncertainties on these numbers are 20 % and 10 %, respectively.

4.3.6. *Summary of the analysis at the Huygens landing site*

We have fitted a VIMS spectrum of the Huygens Landing Site (HLS) constructed from TB measurements by using the DISR-derived aerosol model (Tomasko et al. 2008b) in terms of optical depth profiles and phase function (using their phase function above 80 km for the whole atmosphere). For the single scattering albedo ω_0, we used the DISR-derived haze/mist bimodal description shortward of 1.28 μm. Longward, we used a single value for ω_0, spectrally adjusted to match the wings (and to a lesser extent the cores) of the strong methane bands. The retrieved ω_0 spectrum is slightly different from model calculations using the optical constants of Khare et al. (1984), modified by Rannou et al. (2010), and the haze fractal structure derived from DISR. In particular, we find a more progressive decrease of ω_0 over 1.3-2.5 μm, and the drop of ω_0 near 2.6 μm is found to occur about 0.1 μm before that expected from the tholins of Khare et al. (1984). In the fitting process, the far wing behavior of the strong CH_4 lines was adjusted, in the form of a χ factor. Using initially χ proportional to $\exp(-\Delta\sigma/120)$ beyond 26 cm^{-1} from line center, where $\Delta\sigma$ is the distance from line center in cm^{-1}, we found it suitable to match the 1.1-1.8 μm and 2.4-3.2 μm regions but had to modify it for the 2-μm window (i.e. for the wings of the pentad CH_4 lines at 2.3 μm) and used an $\exp(-\Delta\sigma/200)$ dependence. To complement the near-infrared range shortward of 1.26 μm, we added a band model built directly from ULVS/ULIS measurements (Karkoschka & Tomasko 2010) with a -0.016 km^{-1} $amagat^{-1}$ correction longward of 1.0 μm.

The model permits us to recover surface albedos over 0.88-1.6 μm at the HLS in close agreement with those determined from DISR (Jacquemart et al. 2008). At longer wavelengths, we find surface albedos of 0.11±0.01 at 2.0 μm, 0.05±0.02 at 2.7-2.8 μm and 0.03±0.01 at 5 μm (i.e. 10 %, 40 %, and 33 % uncertainties, respectively) These results are largely consistent with the study of Griffith et al. (2012), except at 2.0 μm, where their much lower value (0.05±0.03) is the result of their much higher assumed single scattering albedo and different line wing description.

5. Evolution of the aerosol distribution from 2004 to 2010

With the atmospheric model constrained by the HLS spectrum, we now address two additional issues. We first study the time evolution of the aerosol distribution, using a selection of 22 VIMS whole-disk images, taken over Oct. 2004 – June 2010 (see Section 2). This study complements that of Rannou et al. (2010) who focused on the haze latitudinal structure, from detailed analyses of two VIMS observations. From a TA image, the authors observed a well marked North-South asymmetry (NSA), with the haze opacity increasing by a factor of ~3 from the South Pole to the Equator, then keeping a constant value up to 30 N, and a factor-of-two decrease over 30N-60N. Our study also complements the pre-Cassini studies on the NSA and its seasonal evolution (Lorenz et al. 1999, 2001 in the visible and Hirtzig et al. 2006 in the infrared).

We quantified the aerosol evolution by means of a single adjustable parameter, namely the overall aerosol extinction in each region, expressed in units of the DISR-measured extinction (Tomasko et al. 2008b), and holding all other model parameters (in particular haze single scattering albedo and phase function) fixed. Results for each of the 22 VIMS cubes are tabulated in Table 2 and shown in Fig. 9, where the haze scaling factor defined in this manner is shown in color code as a function of time for the three (E, N, S) areas. We find that generally moderate departures from the DISR opacities account for most of the spectra. Throughout the 2004-2008 time interval, the Northern hemisphere appears haze-enriched (scaling factor 1-1.3), while the Southern one is depleted (scaling factor 0.7-1) compared to the reference (An exception is the T7 N area indicating a low haze loading (0.8). Yet a progressive decline of the haze loading is visible in the Northern hemisphere.

The 2009-2010 period is characterized by a progressive decline of the Northern hemisphere haze, reducing the North-South asymmetry, whereas the Southern hemisphere shows at most a marginal opacity enhancement. The right part of Fig. 9 shows the latitudinal variation of the haze from data acquired in 2004, 2007 and 2010. In spite of the steady decrease of the Northern haze, it is clear that the NSA reversal had not occurred by the end of the dataset we considered, i.e. mid-2010. As Titan Northern Spring Equinox occurred on August 2009, this indicates a minimum shift of the NSA reversal by 1 year after the Equinox. This is consistent with the fact that the previous NSA reversal occurred over 1997-2000, i.e. 2-5 years after the October 1995 Northern fall equinox (Lorenz et al. 2001). This lagged behavior contrasts with that of the detached haze layer, whose altitude has undergone a drastic decrease (from 500 to 350 km) over a ~1-year period precisely centered on the Equinox (West et al. 2011). In addition, other recent papers based on Cassini studies of CIRS spectra indicate that the reversal of the polar-most NSA component has begun again around mid-2012 and that the atmospheric content enhancement is setting in the South pole at a rapid pace (Jennings et al. 2012; Bampasidis et al. 2012, Teanby et al. 2012). Jennings et al. (2012) in particular show the apparition of a specific haze/cloud component visible in the CIRS spectra in the South pole and its decrease in the North polar region specifically since July 2012.

6. Surface albedos of specific landmarks

Titan’s surface variegation has been revealed by the Cassini mission, and surface units have been classified on the basis of albedo and spectral classifications of the VIMS data. As indicated in Section 2, by considering two specific VIMS cubes, we studied the diversity of surface units by analyzing examples of “dark” and “bright” regions including the “brown” and “blue” categories, as well as the unusual case of Tui Regio. As in the previous Section addressing the aerosol evolution, the atmospheric model was kept fixed, except for the adjustable aerosol extinction in each region. Results, expressed again in DISR extinction units, are given in Table 2. We then determined surface albedos in each spectral window for each of the five regions. As warranted by the construction of the model, which assumes that the surface albedo does not change rapidly with wavelength, the data do not provide more than one albedo value per spectral window. Error bars on the retrieved albedos include (i) random errors due to noise in the data (ii) random errors due to propagation of haze retrieval errors (iii) systematic errors due to model, resulting e.g. from uncertainties due to far-wing opacity. When considering albedo differences between two regions (see below), the first two sources of errors were combined quadratically. In contrast, at 2.0, 2.7, and 5 μm, where systematic uncertainties dominate the error budget, the 10 %, 40 % and 33 % uncertainties pertaining to individual regions were also applied when dealing with albedo differences.

6.1. Qualitative results

Figure 10 (left panel) displays the surface albedos we retrieved for the Huygens landing site, with comparison to results by Jacquemart et al. (2008) and Griffith et al. (2012). As indicated above, our values are in close agreement with those of Jacquemart et al. (2008) shortward of 1.6 μm. With the exception of 2.0 μm, our results are also reasonably consistent with those of Griffith et al. (2012a), although we generally find somewhat brighter albedos than they do beyond 0.94 µm. This is not easy to explain given that our selection of the HLS spectrum has a somewhat lower I/F value (by 0.010+/-0.005, depending on the windows) than theirs, which presumably is due to the fact that the Griffith et al. (2012a) selection includes regions brighter than the dark HLS one. As discussed above, the large discrepancy on the 2-μm albedo (0.05±0.03 from Griffith et al. (2012) vs 0.11±0.01 in this work) is the result of their much higher single scattering albedo and different line wing description in this window.

As a result, our albedo spectrum does not show the steady decline with wavelength that led Griffith et al. (2012) to stipulate that the spectrum of Titan's HLS is consistent with that of Ganymede, i.e. strongly suggestive of exposed water ice. Evidence for water ice has been also claimed in earlier studies of full-disk Titan spectra observed from Earth (Coustenis et al. 1995, Griffith et al. 2003). Yet it is a somewhat surprising result, as Titan's surface is constantly rained over by photochemical products of methane, leading to an accumulation of hundreds meters of organic sediments over 4.5 Gyr. Griffith et al. (2012) note that aeolian and fluvial erosion, for which there is evidence on Titan, are likely to wash out these sediments at places, and that this is perhaps the case at the HLS through the erosion that formed its flood plain, eventually leaving exposed water ice. Instead, our analysis is inconsistent with a strong 2 μm absorption, and therefore with the presence of water ice on the surface at the HLS.

The right panel of Figure 10 shows surface albedos for the five regions of interest selected, compared to the HLS surface albedo spectrum. As expected, at all wavelengths, the three "bright" regions have much larger albedos than the three (including the HLS) "dark" regions. Surface albedos in the bright areas, especially "bright blue and bright Tui", reach 0.25-0.4 over 1-2 μm, vs 0.05-0.2 for the dark areas. The 5-μm albedo shows the largest variation: (0.0-0.05 for dark RoI, ~0.07 for bright ones, and ~0.15 for Tui Regio). Within a given "family" ("bright" or "dark"), however, the albedo variability is not monotonic. "Bright brown" has an albedo similar to "bright blue" at 3 and 5 μm, but is significantly less bright at 1-2 μm. "Bright Tui" has an albedo comparable to "bright blue" at 0.9-1.6 μm, but is much brighter at 2 μm and longward. Similarly, "dark blue" is significantly brighter than "dark brown" shortward of 1.4 μm and the trend reverses above 1.8 μm. All these behaviors are expected given that the "blue" criterion is defined by a high 1.28 μm / 2.03 μm ratio. Below, we try to interpret them in terms of composition variability between the different units.

6.2. Interpretation in terms of surface composition variability

Interpreting Titan's surface albedo in terms of an "absolute" surface composition has been so far rather deceiving and leading to controversial results. One of the few seemingly significant pre-Cassini results, namely the presence of exposed water (Coustenis et al. 1995, Griffith et al. 2003) was challenged by the relatively featureless DISR spectrum over 860-1600 nm (Tomasko et al. 2005, Jacquemart et al. 2008, Schröder and Keller 2008). The latter showed a weak band centered at 1.50-1.58 μm, but attributing this band to H_2O is not too convincing in the absence of companion bands at 1.04 and 1.25 μm. Based on VIMS data, McCord et al. (2006) found the spectrum of bright regions to be inconsistent with water ice alone (based on the lack of a pronounced 2-μm absorption in their spectra), although the spectrum of dark areas was found to agree with a mix of water ice and some non-ice darker component. We rather find that near-infrared spectra of “dark” and “bright” regions differ *to first order* about the absolute reflectance level, rather than about the different spectral shape, and, at odds with Griffith et al. (2012), we find that even the dark regions, as exemplified by the Huygens landing site, lack the 2-μm absorption.

Rather than attempting once more to interpret absolute spectra, we here focus on the differential behavior of the different RoIs Working on differences of spectra, we are less sensitive to systematic modeling errors, such as the representation of the methane opacity. For this we compare the albedo spectrum of each RoI with the HLS, searching to interpret the difference in terms of an excess/lack of a given compound. Specifically, we considered four candidate materials: water ice (with 100- and 1,000-μm sized grains), and tholins (1- and 30-μm size). Although the literature provides spectral information for a wealth of other candidates, such as CO_2 (Quirico and Schmitt 1997; Quirico et al. 1999), CH_4 (Grundy et al. 2002), NH_3 (Schmitt et al. 1998), bitumen (asphaltite - kerite - anthraxolite), and other kinds of “tholins” from brown to yellow (Coll et al. 1999; Bernard et al. 2006), we deem it sufficient to restrict us to the most likely or most discussed compounds. The albedo spectrum of each material A_{material} was calculated from *Spectrimag* (Douté and Schmitt 1998), using the Khare et al. (1984) optical constants for tholins (modified by Rannou et al. 2010), and Grundy and Schmitt (1998) and Schmitt et al. (1998) for water ice. Then, for each candidate material, the difference spectrum of each RoI was modeled as:

$$A_{\text{RoI}} - A_{\text{HLS}} = \alpha\,(A_{\text{material}} - A_{\text{HLS}}),$$

where α, representing the excess/lack of the considered material in the RoI, was determined by least-square fitting, with goodness of the fit characterized by χ^2. For example, $\alpha = 20$ % means that the spectrum of the RoI can be viewed as the sum of 80 % of the HLS spectrum and 20 % of the spectrum of the considered material. Whenever pure materials turned out to be insufficient to explain the spectral differences, we also considered linear combinations thereof.

The top left panel of Fig. 11 shows the albedo spectrum for each of the four materials, compared to the HLS surface spectrum. The other panels in this figure show the result of this "differential fitting", for each of the five RoIs called "Bright Tui", "Bright Brown", "Bright Blue", "Dark Brown", and "Dark Blue". The χ^2_r (reduced χ^2, i.e. the chi-squared divided by the number of fitted points) indicate which of the surface materials permits the best fit. As can be expected dark areas appear very similar to the HLS. For the "Dark Brown" unit, best fits are achieved for extremely small changes of the surface composition with respect to the HLS, at the level of 1 % to several percent only, with variations in small tholin content formally providing the best fit. The "Dark Blue" spectrum is best fitted with a combined excess of 100-μm water ice (+12 %) and lack of 1-μm tholin (- 5 %) (as suspected by Rodriguez et al., 2006); again, these are small compositional changes from the HLS. Bright regions require larger variations in composition. Best fits for "Bright Brown" and "Bright Tui" are achieved with an excess of small tholins (+15 and +26 %, respectively). Finally similar to "Dark Blue", fitting the "Bright Blue" spectrum requires mixtures as opposed to pure materials. We found that a reasonable match could be obtained by replacing 60 % of the Huygens albedo by 40 % of 30-μm tholins and 20 % of 100-μm water ice. Overall bright regions are found to contain more tholins than dark areas, and "blue" regions point to an increased abundance of small grains of H_2O ice.

As a conclusion, and even if the presence of water ice as a major surface constituent or a complement to tholin coating (a suggested previously by e. g. Coustenis et al. 1995; Griffith et al. 2003; Lellouch et al. 2004; Tomasko et al. 2005; Negrão et al. 2006; Rodriguez et al. 2006; McCord et al. 2008; Le Mouélic el al. 2008; Griffith et al. 2012), still remains to be definitively confirmed, we find trends that blue regions, both bright and dark can be simulated by a greater water ice content than their counterparts. In general, bright regions seem to be more tholin-rich than dark regions. This is the case, in particular, of Tui Regio, a cryovolcanic candidate, which shows a large excess of small-sized tholins but no remarkable spectral signature.

7. Summary

Combining advanced technique measurements (DAS and CRDS) and theoretical calculations (expansion of the effective Hamiltonian to high order), extensive methane line lists have recently become available, covering the infrared range longward of 1.263 µm.

Taking advantage also of their overlap and complementarity with methane absorption coefficients derived from the in situ Huygens/DISR measurements, it is now possible to fit the complete Cassini/VIMS infrared spectra (0.8-5.2 μm) of Titan in a realistic manner. In this paper we have illustrated these advances in three directions: (i) fitting a VIMS spectrum of the Huygens landing site confirms the spectral behavior of the surface albedo measured by DISR over 0.9-1.6 μm and permits its extension to longer wavelengths (ii) monitoring of the time evolution of the haze over 2004-2010 shows the progressive decline of the haze inventory in the Northern hemisphere (but not yet the reversal of the North South Asymmetry) (iii) comparing surface albedos in different areas, including the “dark” vs “bright” and “blue” vs “brown” units, indicates plausible sources for the spectral/albedo diversity, especially a likely increased abundance of tholins in the bright regions and a possible enhancement of the water ice content in blue units.

While a massive analysis of the entire VIMS data seems now in order, one should emphasize that missing key spectroscopic parameters still represent important limitations for these studies. Line lists for CH_4 must be extended to shorter wavelengths. Perhaps even more urgently needed is an independent knowledge of the far wing absorption properties of methane, in temperature/pressure conditions relevant to Titan and for the various band complexes independently (pentad, octad, tetradecad, etc…), as those appear of critical importance in controlling opacity in window regions. CH_3D is also an important absorber throughout the near-infrared and line lists, currently available only in the interval 1.26-1.71 μm and beyond 2.2 μm, must be expanded to other wavelengths.

Despite these advances, spectroscopic studies of Titan’s surface have been for a long time – and are still to some extent – rather challenging to interpret, and hence the fundamental question of what surface material(s) is/are responsible for the near-infrared spectrum has not received an unquestionable answer. In this respect, both DISR and VIMS are limited by their modest resolving powers (300 at best), preventing the detection of possible narrow, diagnostic spectral features within the methane windows. Yet, a number of sparse but high-quality Earth-based (Keck, VLT) or Earth-orbit (ISO) datasets are available, covering Titan’s near-infrared spectrum at spectral resolutions 5-10 times better, and reanalysis of all of these data with state-of-the-art methane description (as examples shown in Campargue et al. 2012) now seems warranted. For the future, a near-infrared spectro-imager with enhanced spectral capabilities on a dedicated Titan Orbiter, ideally complemented by a similar instrument on a Titan Lander or aerostat, would be best suited for investigating the nature of Titan’s surface.

Acknowledgments

The authors acknowledge financial support from the French “Agence Nationale de la Recherche” (ANR Project: CH4@Titan) and from the “Groupe de Recherche International SAMIA” network. VB also acknowledges the support of the “OSU THETA de Franche-Comté Bourgogne” and the “SpecMo” GdR number 3152 of the CNRS. The authors also want to acknowledge Le Wang and L. Brown for fruitful collaborations, S. Vinatier, X. Thomas, L. Daumont, L. Regalia and A. Solomonidou for constructive discussions and advice.

References

Albert, S., Bauerecker, S., Boudon, V., Brown, L.R., Champion, J.-P., Loëte, M., Nikitin, A., Quack, M., 2009. Global analysis of the high resolution infrared spectrum of methane $^{12}CH_4$ in the region from 0 to 4800 cm^{-1}. Chem. Phys. 356, 131-46.

Atreya, S.K., Adams, E.Y., Niemann, H.B., Demick-Montelara, J.E., Owen, T.C., Fulchignoni, M., Ferri, F., Wilson, E.H., 2006. Titan’s methane cycle. Planet. Space Sci. 54, 1177-1187.

Bailey, J., Ahlsved, L., Meadows, V.S., 2011. The near-IR spectrum of Titan modeled with an improved methane line list. Icarus 213, 218–232.

Bampasidis, G., et al., 2012. Thermal and temperature structure variations in Titan’s stratosphere during the Cassini mission. Astroph. J. 760, Article id. 144.

Barnes, J.W. et al., 2005. A 5-micron-bright spot on Titan: Evidence for surface diversity. Science 310, 92-95.

Barnes, J.W., Brown, R.H., Soderblom, L., Buratti, B.J., Sotin, C., Rodriguez, S., Le Moue lic, S., Baines, K.H., Clark, R., Nicholson, P., 2007. Global-scale surface spectral variations on Titan seen from Cassini/VIMS. Icarus 186, 242–258.

Bernard, J.-M., Quirico, E., Brissaud, O., Montagnac, G., Reynard, B., McMillan, P., Coll, P., Nguyen, M.-J., Raulin, F., Schmitt, B., 2006. Reflectance spectra and chemical structure of Titan's tholins: Application to the analysis of Cassini Huygens observations. Icarus 185, 301-307.

Bézard, B., Nixon, C.A., Kleiner, I., Jennings, D.E., 2007. Detection of $^{13}CH_3D$ on Titan. Icarus 191, 397-400.

Boudon, V., Rey, M., Loete, M., 2006. The vibrational levels of methane obtained from analyses of high-resolution spectra. J. Quant. Spectrosc. Radiat. Transfer 98, 394–404.

Brodbeck, C., Bouanich, J.-P., Nguyen-Van-Thanh, Hartmann, J.-M., Khalil, B., Le Doucen, R., 1994. Absorption of radiation by gases from low to high pressures. II. Measurements and calculations of CO infrared spectra. J. Phys. II France 4, 2101-2118.

Brown, L.R., et al., 2003. Methane line parameters in HITRAN. J. Quant. Spectrosc. Radiat. Trans. 82, 219-238.

Campargue, A., et al., 2012. An empirical line list for methane in the 1.26-1.71 μm region for planetary investigations (T=80-300 K). Application to Titan. Icarus 219, 110-128.

Coll, P., Coscia, D., Smith, N., Gazeau, M.-C., Ramirez, S.I., Cernogora, G., Israël, G., Raulin, F., 1999. Experimental laboratory simulation of Titan's atmosphere: aerosols and gas phase. Planet. Space Sci. 47, 1331-1340.

Coustenis, A., Lellouch, E., Maillard, J.P., McKay, C.P., 1995. Titan’s surface: Composition and variability from its near-infrared albedo. Icarus 118, 87–104.

Daumont, L. et al., 2013. New assignments in the 2 μm transparency window of the $^{12}CH_4$ Octad band system. J. Quant. Spectrosc. Radiat. Transfer 116, 101-109.

de Bergh, C., et al., 2012. Applications of a new set of methane line parameters to the modeling of Titan’s spectrum in the 1.58 micron window. Planet. Space Sci. 61, 85–98.

Douté, S., Schmitt, B., 1998. A multilayer bidirectional reflectance model for the analysis of planetary surface hyperspectral images at visible and near-infrared wavelengths. J. Geophys. Res. 103, 31367-31390.

Fulchignoni, M., et al., 2005. In situ measurements of the physical characteristics of Titan's environment. Nature 438, 785-791.

Griffith, C.A., Owen, T., Wagener, R., 1991. Titan’s surface and troposphere, investigated with ground-based, near-infared observations. Icarus 93, 362–378.

Griffith, C.A., Owen, T., Geballe, T.R., Rayner, J., Rannou, P., 2003. Evidence for the exposure of water ice on Titan’s surface. Science 300, 628–630.

Griffith, C.A., Doose, L., Tomasko, M.G., Penteado, P.F., See, C., 2012. Radiative transfer analyses of Titan’s tropical atmosphere. Icarus 218, 975–988.

Grundy, W.M., Schmitt, B., 1998. The temperature-dependent near-infrared absorption spectrum of hexagonal H_2O ice. J. Geophys. Res. 103, 25809-25822.

Grundy, W.M., Schmitt, B., Quirico, E., 2002. The temperature-dependent spectrum of methane ice I between 0.7 and 5 μm and opportunities for near-infrared remote thermometry. Icarus 155, 486-496.

Hirtzig, M., et al., 2006. Monitoring atmospheric phenomena on Titan. Astron. Astrophys. 456, 761-774.

Irwin, P.G.J., Sromovsky, L.A., Strong, E.K., Sihra, K., Bowles, N., Calcutt, S.B., Remedios, J.J., 2006. Improved near-infrared methane band models and k-distribution parameters from 2000 to 9500 cm-1 and implications for interpretation of outer planet spectra. Icarus 181, 309–319.

Jacquemart, D., Lellouch, E., Bézard, B., de Bergh, C., Coustenis, A., Lacome, N., Schmitt, B., Tomasko, M., 2008. New laboratory measurements of CH_4 in Titan's conditions and a reanalysis of the DISR near-surface spectra at the Huygens landing site. Planet. Space Sci. 56, 613-623.

Jennings, D. E., et al., 2012. Seasonal disappearance of far-infrared haze in Titan’s stratosphere. Astroph. J. 754, L3.

Karkoschka, E., Tomasko, M.G., 2010. Methane absorption coefficients for the jovian planets from laboratory, Huygens, and HST data. Icarus 205, 674-694.

Khare, B.N., Sagan, C., Arakawa, E.T., Suits, F., Callcott, T.A., Williams, M.W., 1984. Optical constants of organic tholins produced in a simulated Titanian atmosphere – From soft X-ray to microwave frequencies. Icarus 60, 127– 137.

Lafferty, W.J., Solodov, A.M., Weber, A., Olson, Wm.B., Hartmann, J.-M., 1996. Infrared collision-induced absorption by N_2 near 4.3 μm for atmospheric applications. Appl. Opt. 35, 5911-5917.

Le Mouélic, S., et al., 2008. Mapping and interpretation of Sinlap crater on Titan using Cassini VIMS and RADAR data. J. Geophys. Res. 113, E04003.

Lellouch, E., Coustenis, A., Sebag, B., Cuby, J.-G., Lopez-Valverde, M., Fouchet, T., Crovisier, J., Schmitt, B., 2003. Titan’s 5-micron window: observations with the Very Large Telescope. Icarus 162, 125-142.

Lellouch, E., Schmitt, B., Coustenis, A., Cuby, J.-G., 2004. Titan’s 5-micron lightcurve. Icarus 168, 209-214.

Lopez-Valverde, M.A., Lellouch, E., Coustenis, A., 2005. Carbon monoxide fluorescence from Titan’s atmosphere. Icarus 175, 503-521.

Lorenz, R.D., Lemmon, M.T., Smith, P.H., Lockwood, G.W., 1999. Seasonal Change on Titan observed with the Hubble Space Telescope WFPC-2. Icarus 142, 391-401.

Lorenz, R.D., Young, E.F., Lemmon, M.T., 2001. Titan's smile and collar: HST Observations of seasonal change 1994-2000. Geophys. Res. Lett. 28, 4453-4456.

Lyulin, O.M., Nikitin, A.V., Perevalov, V.I., Morino, I., Yokota, T., Kumazawa, R., Watanabe, T., 2012. Measurements of N_2- and O_2-broadening and shifting parameters of methane spectral lines in the 5550-6236 cm^{-1} region. J. Quant. Spectrosc. Radiat. Transfer 110, 654-668.

McCord, T.B., et al., 2006. Composition of Titan’s surface from Cassini VIMS. Planet. Space Sci. 54, 1524-1539.

McCord, T.B., et al., 2008. Titan’s surface: Search for spectral diversity and composition using the Cassini VIMS investigation. Icarus 194, 212-242.

McKay, C.P., Pollack, J.B., Courtin, R., 1989. The thermal structure of Titan's atmosphere. Icarus 80, 23-53.

Negrão, A., Coustenis, A., Lellouch, E., Maillard, J.-P., Rannou, P., Combes, M., Schmitt, B., McKay, C. P., Boudon, V., 2006. Titan’s surface albedo from near-infrared CFHT/FTS spectra: modeling dependence on the methane absorption. Planet. Space Sci. 54, 1225-1246.

Nelson, R.M. et al., 2006. Photometric properties of Titan's surface from Cassini VIMS: Relevance to Titan's hemispherical albedo dichotomy and surface stability. Planet. Space Sci. 54, 1540-1551.

Nelson, R.M. et al., 2009a. Photometric changes on Saturn's Titan: Evidence for active cryovolcanism. Geophys. Res. Lett. 36, L04202.

Nelson, R. M. et al., 2009b. Saturn's Titan: Surface change, ammonia, and implications for atmospheric and tectonic activity. Icarus 199, 429-441.

Niemann, H.B., Atreya, S.K., Demick, J.E., Gautier, D., Haberman, J.A., Harpold, D.N., Kasprzak, W.T., Lunine, J.I., Owen, T.C., Raulin, F., 2010. Composition of Titan’s lower atmosphere and simple surface volatiles as measured by the Cassini-Huygens probe gas chromatograph mass spectrometer experiment. J. Geophys. Res. 115, E12006.

Nikitin, A., Brown, L.R., Féjard, L., Champion, J.-P., Tyuterev, Vl.G., 2002. Analysis of the CH_3D Nonad from 2000 to 3300 cm^{-1}. J. Mol. Spectrosc. 216, 225-251.

Nikitin, A., Champion, J-P., Brown, L.R., 2006. Preliminary analysis of CH_3D from 3250 to 3700 cm^{-1}. J. Mol. Spectrosc. 240, 14–25.

Nikitin, A.V., Thomas, X., Régalia, L., Daumont, L., Von der Heyden, P., Tyuterev, Vl. G., Wang, L., Kassi, S., Campargue, A., 2011. Assignment of the $5\nu_4$ and $\nu_2+4\nu_4$ band systems of $^{12}CH_4$ in the 6287-6550 cm^{-1} region. J. Quant. Spectrosc. Radiat. Trans. 112, 28-40.

Nikitin, A.V., Brown, L.R., Sung, K., Rey, M., Tyuterev, Vl.G., Smith M.A.H., Mantz, A.W., 2013. Preliminary modeling of CH_3D from 4000 to 4550 cm^{-1}. J. Quant. Spectrosc. Radiat. Transfer 114, 1-12.

Peck, E.R., Khanna, B.N., 1966. Dispersion of nitrogen. J. Opt. Soc. Am. 56, 1059-1063.

Quirico, E., Schmitt, B., 1997. A spectroscopic study of CO diluted in N_2 ice: Applications for Triton and Pluto. Icarus 128, 181-188.

Quirico, E., Douté, S., Schmitt, B., de Bergh, C., Cruikshank, D.P., Owen, T.C., Geballe, T.R., Roush, T.L., 1999. Composition, physical state, and distribution of ices at the surface of Triton. Icarus 139, 159-178.

Rannou, P., Cours, T., Le Mouélic, S., Rodriguez, S., Sotin, C., Drossart, P., Brown, R., 2010. Titan haze distribution and optical properties retrieved from recent observations. Icarus 208, 850–867.

Rodriguez, S. et al., 2006. Cassini/VIMS hyperspectral observations of the HUYGENS landing site on Titan. Planet. Space Sci. 54, 1510-1523.

Schmitt, B., Quirico, E., Trotta, F., Grundy, W.M., 1998. Optical properties of ices from UV to infrared. In *Solar System Ices*, Dordrecht Kluwer Academic Publishers, Astrophysics and space science library (ASSL) Series, vol no 227, p.199.

Schröder, S.E., Keller, H.U., 2008. The reflectance spectrum of Titan's surface at the Huygens landing site determined by the descent imager/spectral radiometer. Planet. Space Sci. 56, 753-769.

Soderblom, L.A., et al., 2007a. Topography and geomorphology of the Huygens landing site on Titan. Planet. Space Sci. 55, 2015-2024.

Soderblom, L.A. et al., 2007b. Correlations between Cassini VIMS spectra and RADAR SAR images: Implications for Titan’s surface composition and the character of the Huygens Probe landing site. Planet. Space Sci. 55, 2025–2036.

Solomonidou, A., Bampasidis, G., Hirtzig, M., Coustenis, A., Kyriakopoulos, K., St Seymour, K., Bratsolis, E., Moussas, X., 2012. Morphotectonic features on Titan and their possible origin. Planet. Space Sci., in press.

Sromovsky, L.A., Fry, P.M., Boudon, V., Campargue, A., Nikitin, A., 2012. Comparison of line-by-line and band models of near-IR methane absorption applied to outer planet atmospheres. Icarus 218, 1–23.

Teanby, N.A., Irwin, P.G.J., Nixon, C., de Kok, R., Vinatier, S., Coustenis, A., Sefton-Nash, E., Calcutt, S.B., Flasar, F.M., 2012. Active upper-atmosphere chemistry and dynamics from polar circulation reversal on Titan. Nature 491, 732-735.

Tomasko, M.G., et al., 2005. Results from the descent imager/spectral radiometer (DISR) instrument on the Huygens probe of Titan. Nature 438, 765–778.

Tomasko, M.G., Bézard, B., Doose, L., Engel, S., Karkoschka, E., 2008a. Measurements of methane absorption by the descent imager/spectral radiometer (DISR) during its descent through Titan's atmosphere. Planet. Space Sci. 56, 624-647.

Tomasko, M.G., Doose, L., Engel, S., Dafoe, L.E., West, R., Lemmon, M., Karkoschka, E., See, C., 2008b. A model of Titan's aerosols based on measurements made inside the atmosphere. Planet. Space Sci. 56, 669-707.

Ulenikov, O.N., Bekhtereva, E.S., Albert, S., Bauerecker, S., Hollenstein, H., Quack, M., 2010. High resolution infrared spectroscopy and global vibrational analysis for the CH_3D and CHD_3 isotopomers of methane. Mol. Phys. 108, 1209–1240.

Wang, L., Kassi, S., Campargue, A., 2010a. Temperature dependence of the absorption spectrum of CH_4 by high resolution spectroscopy at 81 K: (I) The region of the $2\nu_3$ band at 1.66 µm. J. Quant. Spectrosc. Radiat. Trans. 111, 1130-1140.

Wang, L., Kassi, S., Liu, A. W., Hu, S. M., Campargue, A., 2010b. High sensitivity absorption spectroscopy of methane at 80 K in the 1.58-µm transparency window: temperature dependence and importance of the CH_3D contribution. J. Mol. Spectrosc. 261, 41-52.

Wang, L., Kassi, S., Liu, A. W., Hu, S. M., Campargue, A., 2011. The 1.58-µm transparency window of methane (6150-6750 cm-1): Empirical line list and temperature dependence between 80 K and 296 K. J. Quant. Spectrosc. Radiat. Trans. 112, 937-951.

Wang, L., Mondelain, D., Kassi, S., Campargue, A., 2012. The absorption spectrum of methane at 80 K and 294 K in the icosad (6717–7589 cm^{-1}): Improved empirical line lists, isotopologue identification and temperature dependence. J. Quant. Spectrosc. Radiat. Trans. 113, 47–57.

Weber, M.J., 2003. *Handbook of Optical Materials.* CRC Press, Boca Raton, Florida.

West, R.A., Balloch, J., Dumont, P., Lavvas, P., Lorenz, R., Rannou, P., Ray, T., Turtle, E.P., 2011. The evolution of Titan's detached haze layer near equinox in 2009. Geophys. Res. Lett. 38, L06204.

TABLES :

Table 1: Cassini/VIMS datacubes used in our study. The first set corresponds to datacubes of the Huygens landing site, used for tuning our RT model (Section 4.2) as well as for direct comparison with other models (Section 4). The second set is used for our spatial and temporal monitoring of the aerosol population (Section 5). The last set focuses on cubes showing a variety of diverse terrains, including bright and dark regions (Brown et al. 2009; Barnes et al. 2009). Labels refer to publications using the same cubes: *a* de Bergh et al. (2012), *b* Griffith et al. (2011), *c* Barnes et al. (2007), *d* Solomonidou et al. (2012), *e* Rodriguez et al. (2011).

Huygens site		Aerosol monitoring		Surface terrains	
Cube	Date	cube	date	cube	date
CM 1477491859[a]	TA (26th Oct 2004)	CM 1477457906	TA (26th Oct 2004)	CM 1481619244[c]	TB (13th Dec 2004)
CM 1481624349[b]	TB (13th Dec 2004)	CM 1487070016	T3 (15th Feb 2005)	CM 1514313117[c]	T9 (26th Dec 2005)
		CM 1490951542	T4 (31st Mar 2005)		
		CM 1492332582	T5 (16th Apr 2005)		
		CM 1504738294	T7 (7th Sep 2005)		
		CM 1509136241	T8 (28th Oct 2005)		
		CM 1514284191	T9 (26th Dec 2005)		
		CM 1515980488	T10 (15th Jan 2006)		
		CM 1519685035	T11 (27th Feb 2006)		
		CM 1530486606	T15 (2nd Jul 2006)		
		CM 1539136970	T19 (9th Oct 2006)		
		CM 1557724855	T30 (13th May 2007)		
		CM 1559103132	T31 (29th May 2007)		
		CM 1560489660	T32 (14th Jun 2007)		
		CM 1561870175	T33 (30th Jun 2007)		
		CM 1605798513[d]	T47 (19th Nov 2008)		
		CM 1621669401[e]	T55 (22nd May 2009)		
		CM 1625809619	T58 (9th Jul 2009)		
		CM 1629929753	T61 (25th Aug 2009)		
		CM 1634084887	T62 (12th Oct 2009)		

	CM 1649215526 T67 (6th Apr 2010) CM 1655801953[e] T70 (21st Jun 2010)	

Table 2: Parameters of the Regions of Interest (“RoIs”) used herein: flyby, coordinates, observation angles (incidence “inc”, emergence “emg”, and phase “phs”) and average spatial resolution (“res”). Also given is the aerosol extinction needed to fit the CH_4 bands and wings, expressed as a scaling factor to that measured by Huygens/DISR. See text for further details.

RoI	lat, long	inc	emg	phs	res (km)	haze (%)	RoI	lat, long	inc	emg	phs	res (km)	haze (%)
Huygens (TA)	10°S, 170°	33°	28°	13°	20	103	Huygens (TB)	10°S, 168°	36°	34°	18°	8	100
bright blue (TB)	18°S, 135° W	20°	28°	17°	5	90	bright brown (TB)	23°S, 140°W	14°	26°	17°	5	90
bright Tui (TB)	22°S, 135° W	18°	29°	17°	5	90							
dark blue (T9)	6°S, 47°W	13°	12°	24°	20	100	dark brown (T9)	1°S, 50°W	19°	4°	22°	20	100
TA S	38°S, 158° W	17°	24°	13°	123	90	T30 S	36°S, 125°E	33°	55°	29°	206	70
TA E	8°S, 156°	16	7°	13°	113	100	T30 E	14°S, 143°E	6°	30°	29°	129	90

	W	°										
TA N	20°N, 163° W	46°	35°	13°	137	119	T30 N	22°N, 140°E	35°	6°	28°	112	110
T3 S	49°S, 151° W	29°	46°	20°	328	71	T31 S	34°S, 119°E	36°	51°	23°	180	72
T3 E	16°S, 143° W	8°	13°	19°	218	100	T31 E	11°S, 137°E	12°	22°	23°	125	90
T3 N	16°N, 143° W	38°	19°	19°	220	124	T31 N	31°N, 141°E	44°	21°	23°	123	116
T4 S	25°S, 24°W	40°	27°	57°	128	80	T32 S	34°S, 117°E	36°	43°	15°	199	80
T4 E	3°S, 42°W	31°	28°	57°	115	90	T32 E	2°S, 137°E	14°	6°	15°	154	100
T4 N	28°N, 50°W	53°	43°	57°	131	98	T32 N	32°N, 141°E	44°	30°	14°	176	119
T5 S	34°S, 22°W	42	38°	55°	193	80	T33 S	42°S,	32°	43°	12°	169	80

		°						138°					
T5 E	8°S, 40°W	30°	25°	55°	153	90	T33 E	6°S, 143°	7°	7°	11°	120	95
T5 N	23°N, 52°W	47°	37°	55°	156	103	T33 N	34°N, 139°E	47°	35°	11°	143	115
T7 S	21°S, 35°W	27°	32°	52°	144	80	T47 S	28°S, 72°W	80°	8°	78°	13	105
T7 E	4°N, -8°W	29°	28°	52°	126	90	T47 E	23°S, 79°W	74°	14°	79°	15	84
T7 N	27°N, 67°W	48°	49°	52°	135	80	T47 N	19°S, 86°W	67°	21°	80°	17	70
T8 S	28°S, 148° W	16°	29°	23°	126	84	T55 S	37°S, 37°E	38°	14°	52°	138	73
T8 E	1°S, 143° W	20°	3°	23°	108	100	T55 E	6°S, 34°E	10°	45°	53°	196	76
T8 N	26°N, 146°	47	26°	23°	121	114	T58 S	29°S,	29°	2°	27°	125	74

	W	°						23°E					
T9 S	32°S, 25°W	16°	33°	28°	147	84	T58 E	4°N, 24°E	4°	32°	27°	152	80
T9 E	2°S, 30°W	16°	16°	28°	124	100	T61 S	37°S, 13°E	40°	30°	13°	139	80
T9 N	25°N, 41°W	45°	37°	28°	138	110	T61 E	0°N, 17°E	11°	7°	13°	123	100
T10 S	34°S, 143° W	26°	35°	35°	175	80	T61 N	34°N, 28°E	33°	43°	13°	169	100
T10 E	3°S, 138° W	25°	10°	35°	142	100	T62 S	35°S, 16°E	37°	35°	10°	216	80
T10 N	23°N, 136° W	45°	27°	35°	154	110	T62 E	1°N, 17°E	7°	3°	10°	178	100
T11 S	38°S, 7°W	20°	39°	18°	133	80	T62 N	34°N, 11°E	35°	35°	10°	219	108
T11 E	8°S,	9	9°	18°	102	90	T67 S	42°S,	47°	43°	16°	144	75

	7°W	°						25°E					
T11 N	25°N, 7°W	43°	26°	17°	111	110	T67 E	2°S, 23°	14°	4°	16°	108	100
T15 S	34°S, 13°E	42°	38°	61°	165	73	T67 N	36°N, 24°E	34°	36°	16°	137	100
T15 E	7°S, 28°E	29°	32°	61°	135	90	T70 S	23°S, 127°E	30°	25°	32°	94	72
T15 N	19°N, 39°E	40°	46°	61°	142	107	T70 E	2°S, 128°E	12°	20°	32°	90	90
T19 S	41°S, 3°W	40°	30°	65°	98	73	T70 N	27°N, 130°E	25°	40°	32°	112	95

Table 3: Effect of a 5 % uncertainty on the haze extinction on the retrieved surface albedo

Surface albedo relative error at specific wavelengths (μm)

0.93	1.08	1.28	1.54	1.59	2.03	2.79	5.00
18%	7.5%	3.5%	34 %	6.0%	0.3%	0.3%	0.2%

FIGURES :

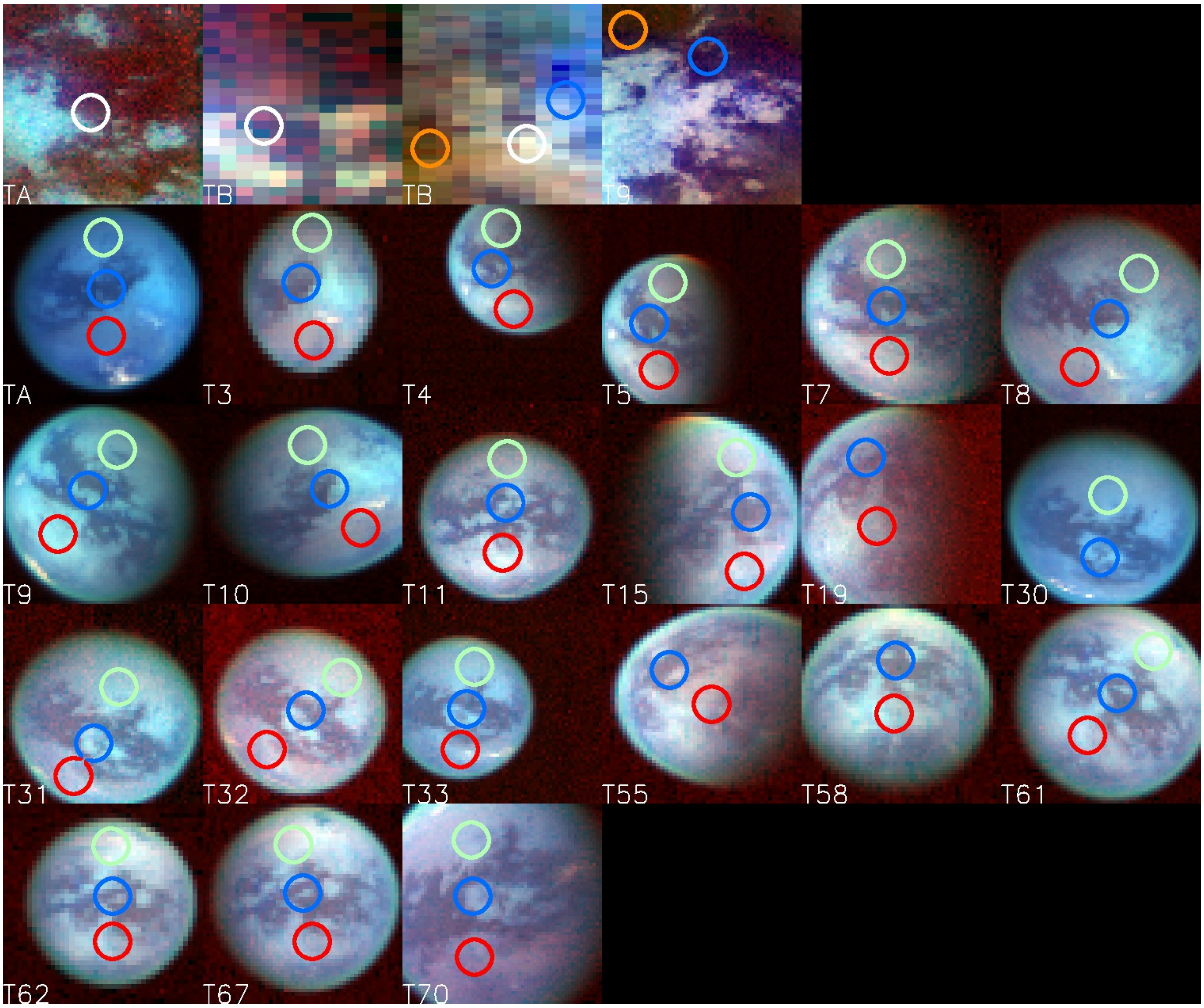

Figure 1. Regions of Interest (RoIs) selected in this work projected on false-color rendering of VIMS data cubes, according to Table 2. Each image is a composite of three VIMS channels (R=5μm, G=2μm, B=1.6μm), with ellipses showing the location of the RoIs. The two upper-left cubes show the Huygens landing site as seen in TA and TB (white ellipses). The two other cubes on the upper line show the five regions selected for surface composition studies: “bright blue” (blue), “bright brown” (orange), and “5-μm bright” (white) areas from TB (CM 1481619244), and “dark blue” (blue) and “dark brown” (orange) from T9 CM 1514313117. The 21 other cubes are used for our temporal and latitudinal monitoring of aerosols, with “southern” (red), “equatorial” (blue), and “northern” (green) RoI, *taken along the same meridian*. All images have been rotated by multiples of 90° so that North is up as much as possible (but not quite, hence some meridians looking tilted or diagonal).

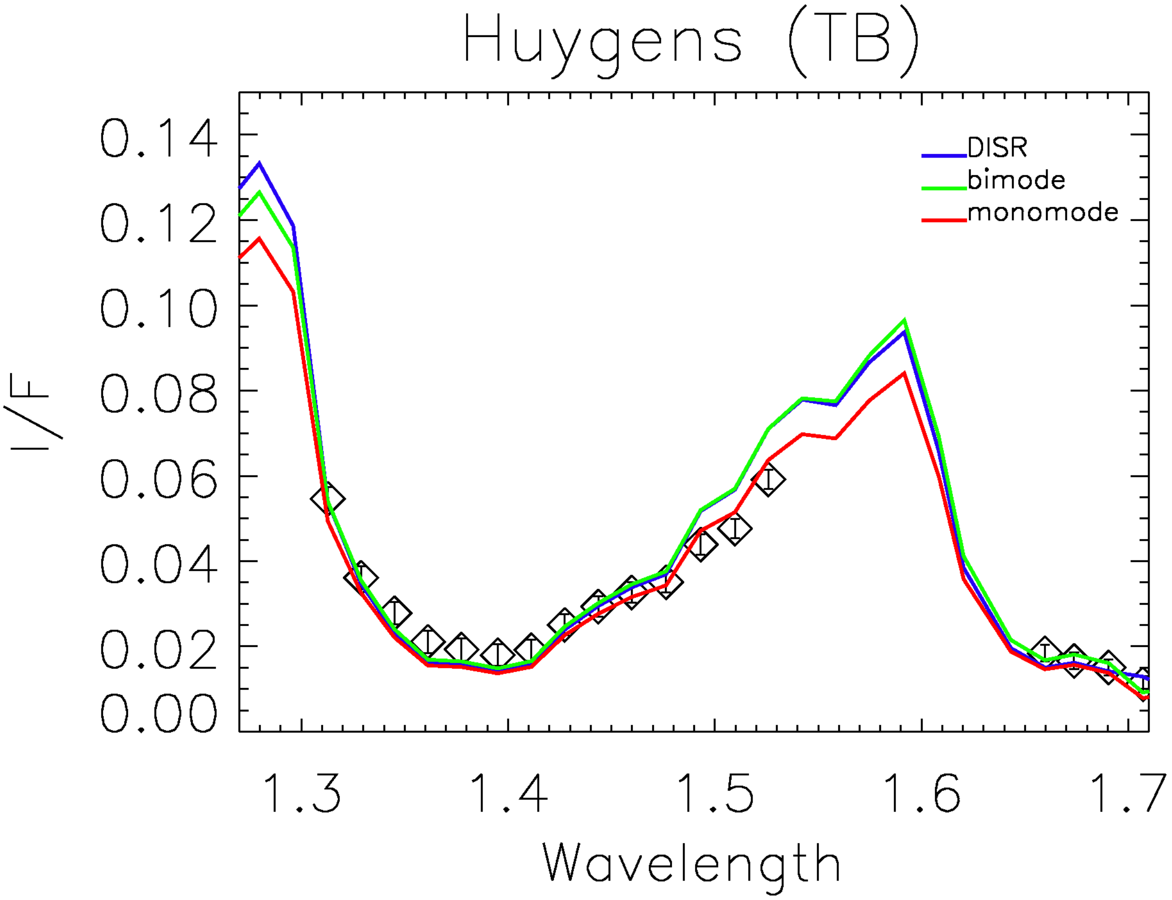

Figure 2. Fit of the TB Huygens landing site spectrum at 1.3-1.7 μm. All simulations shown here use the DISR original aerosol extinction profile and a constant surface albedo of 0.08 (although we focus here only on the fitting of CH_4 bands and wings). Blue curve ("DISR"): aerosol single scattering albedo model from DISR. Green curve ("Bimode"): model in which the aerosol scattering albedo is ω_0 =1.00 above 80 km and ω_0 =0.95 below. Red curve ("Monomode): model with vertically constant ω_0, decreasing from 0.94 at 1.28 μm to 0.92 at 1.58 μm. See text for further explanations.

Figure 3. Determination of aerosol spectral properties. *Upper panel*: synthetic spectra (color curves) for various values of the single scattering albedo between 0.50 and 1.00, using the DISR optical depth profile, compared to the TB VIMS spectrum of the HLS (black points, with error bars). *Middle panel*: Grey points with error bars: single scattering albedo (ω_0) required to fit exactly the VIMS spectrum. Color diamonds: DISR-measured values of ω_0 (red: mist, yellow: haze). Purple curve: ω_0 spectrum calculated for the Khare et al. (1984) optical constants modified by Rannou et al. (2010). Red curve: ω_0 spectrum adopted in this work. Note the yellow curve shortward of 1.28 μm, indicating that the bimodal behavior of the DISR-measured ω_0 is preserved there. *Bottom panel:* Reduced χ^2 maps for the fit of six regions of strong methane absorption at 1.14, 1.40, 1.70, 2.40, 3.10 and 3.60 µm, in the (haze scaling factor F, ω_0) parameter space. Color scale is the same for all six bands. Black contou The figures nds show the solutio

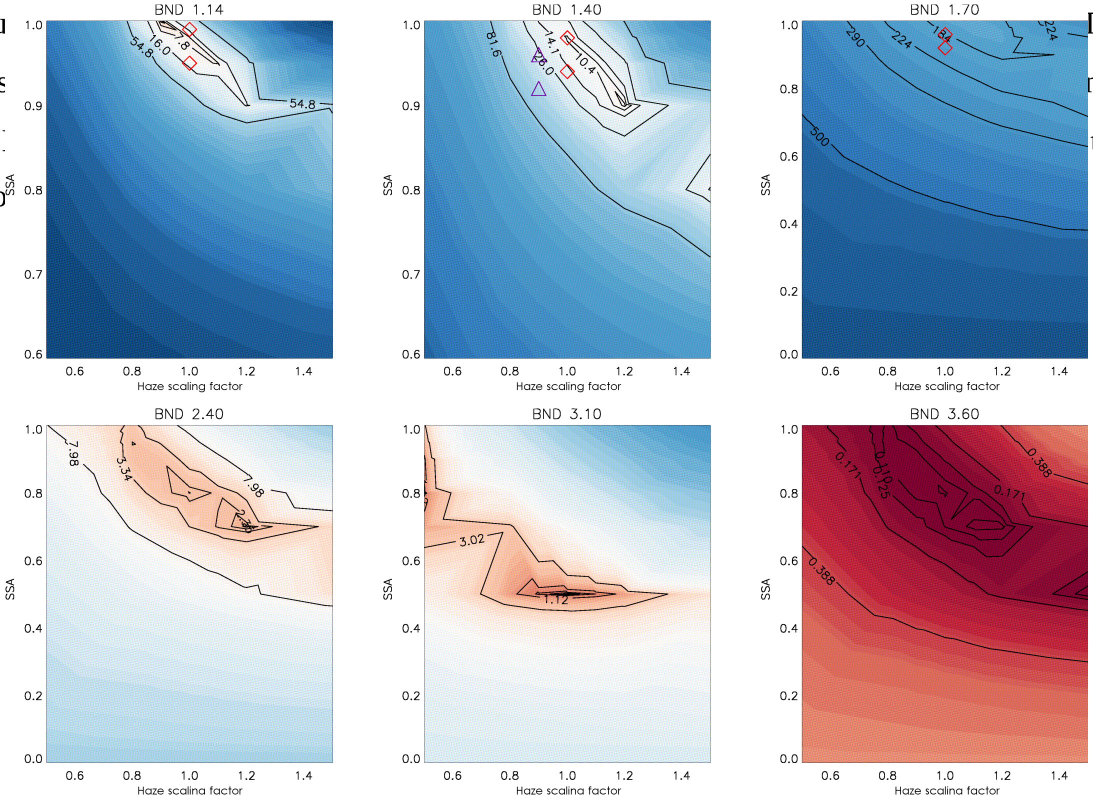

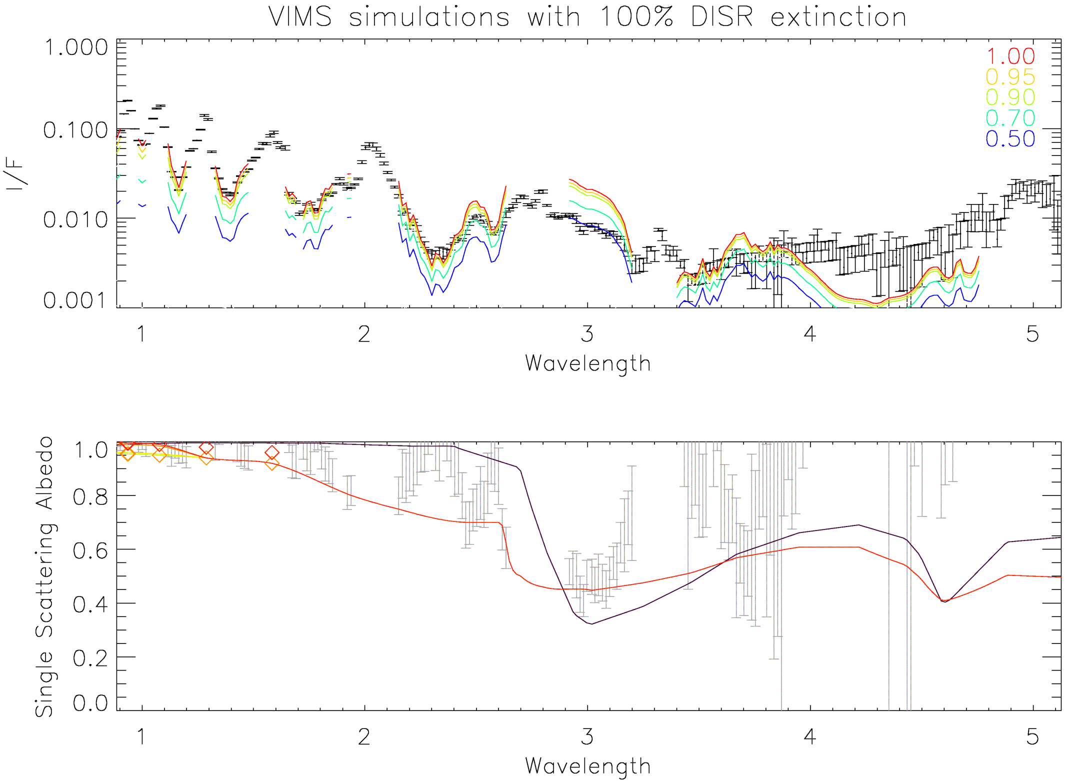VIMS simulations with 100% DISR extinction
1.00
0.95
0.90
0.70
0.50
I/F
1.000
0.100
0.010
0.001
1
2
3
4
5
Wavelength
Single Scattering Albedo
1.0
0.8
0.6
0.4
0.2
0.0
1
2
3
4
5
Wavelength

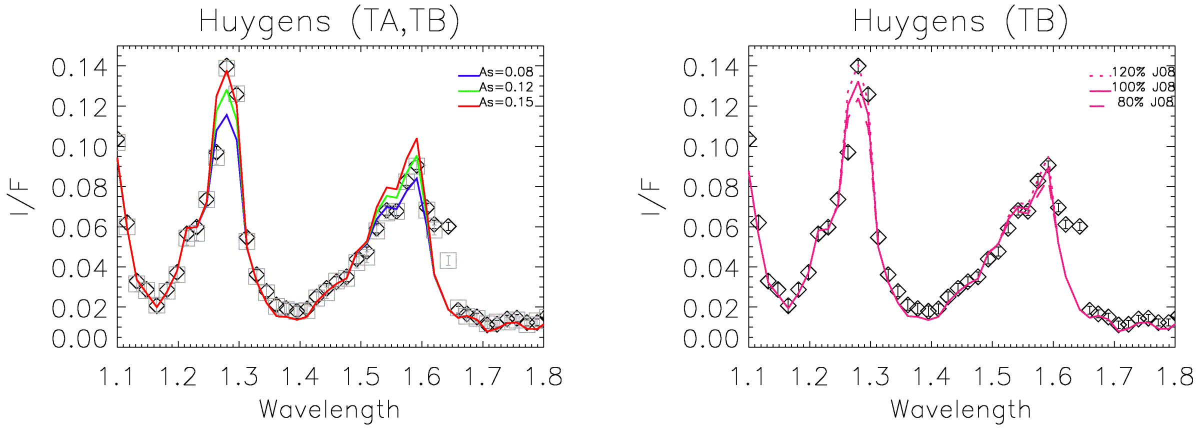

Figure 4. Models of the Huygens landing site spectrum at 1.1-1.8 μm with various surface albedos. *Left.* Models with constant surface albedo of 0.08 (blue), 0.12 (green), and 0.15 (red), compared to spectra from TB (black diamonds) and TA (grey squares), including error bars. *Right:* TB spectrum, compared to models in which the surface albedo spectrum of Jacquemart et al. (2008) is multiplied by 1.2 (dotted line), 1.0 (solid line), and 0.8 (dashed line).

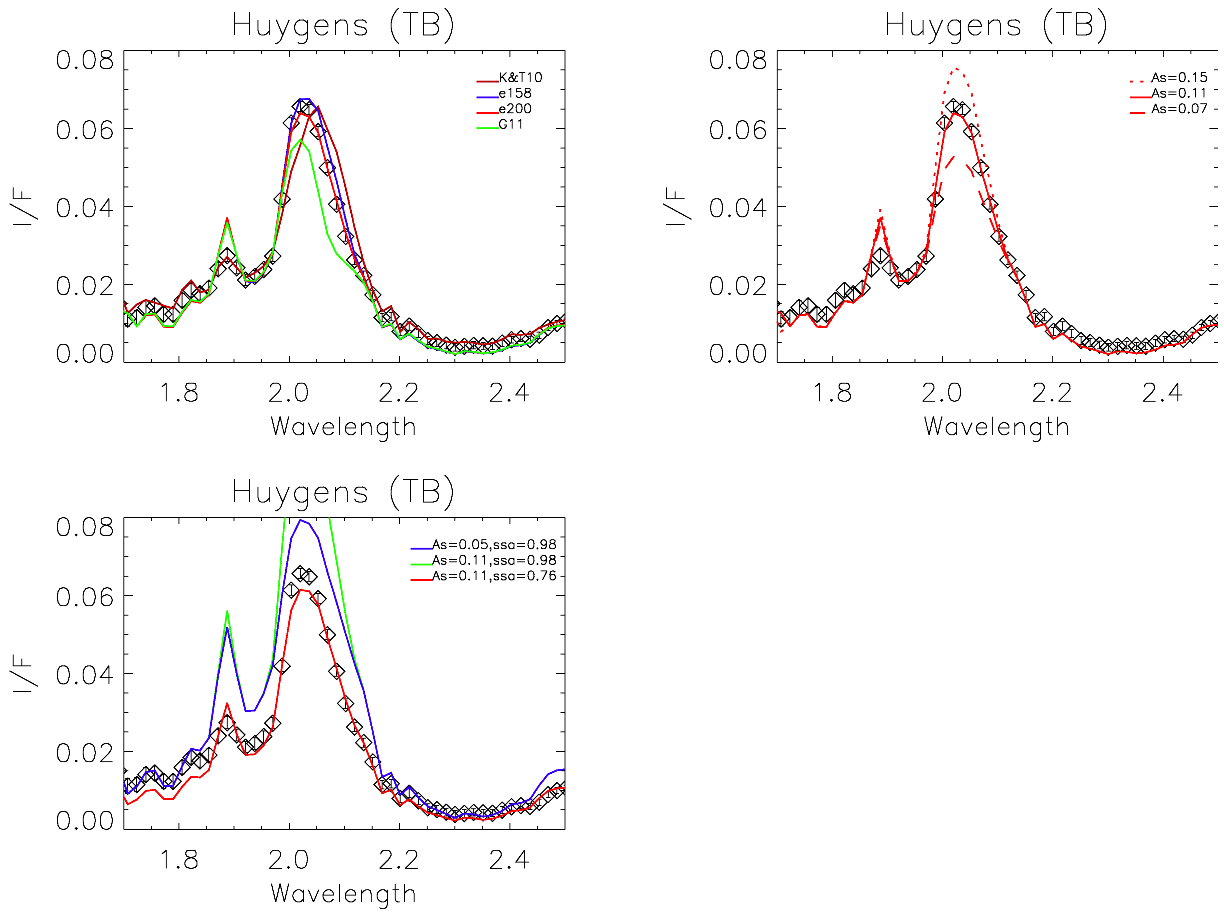

Figure 5. Models of the Huygens landing site spectrum at 1.7 – 2.5 μm. *First panel:* Effect of the treatment of methane opacity, using a surface albedo of 0.11. Brown curve (K&T10): band model Karkoschka & Tomasko (2010). Blue and red curves: calculations based on the line list presented in this work, using sub-lorentzian χ factors proportional to $exp(-\Delta\sigma/158)$ (blue) or $exp(-\Delta\sigma/200)$ (red) beyond 26 cm^{-1} from line center. Green line (G11): same, but using an abrupt absorption cut-off of the Voigt profile at 500 cm^{-1} from line center, instead of a χ-like dampening function. *Second panel*: Calculations using an $exp(-\Delta\sigma/200)$ χ factor and various surface albedos: 0.07 (dashed line), 0.11 (solid line), and 0.15 (dotted line). *Third panel*: Effect of haze single scattering albedo (ω_0) and surface albedo (A_S). Green: $\omega_0 = 0.98$, $A_s = 0.11$. Blue: $\omega_0 = 0.98$, $A_s = 0.05$. Red: $\omega_0 = 0.76$, $A_s = 0.11$.

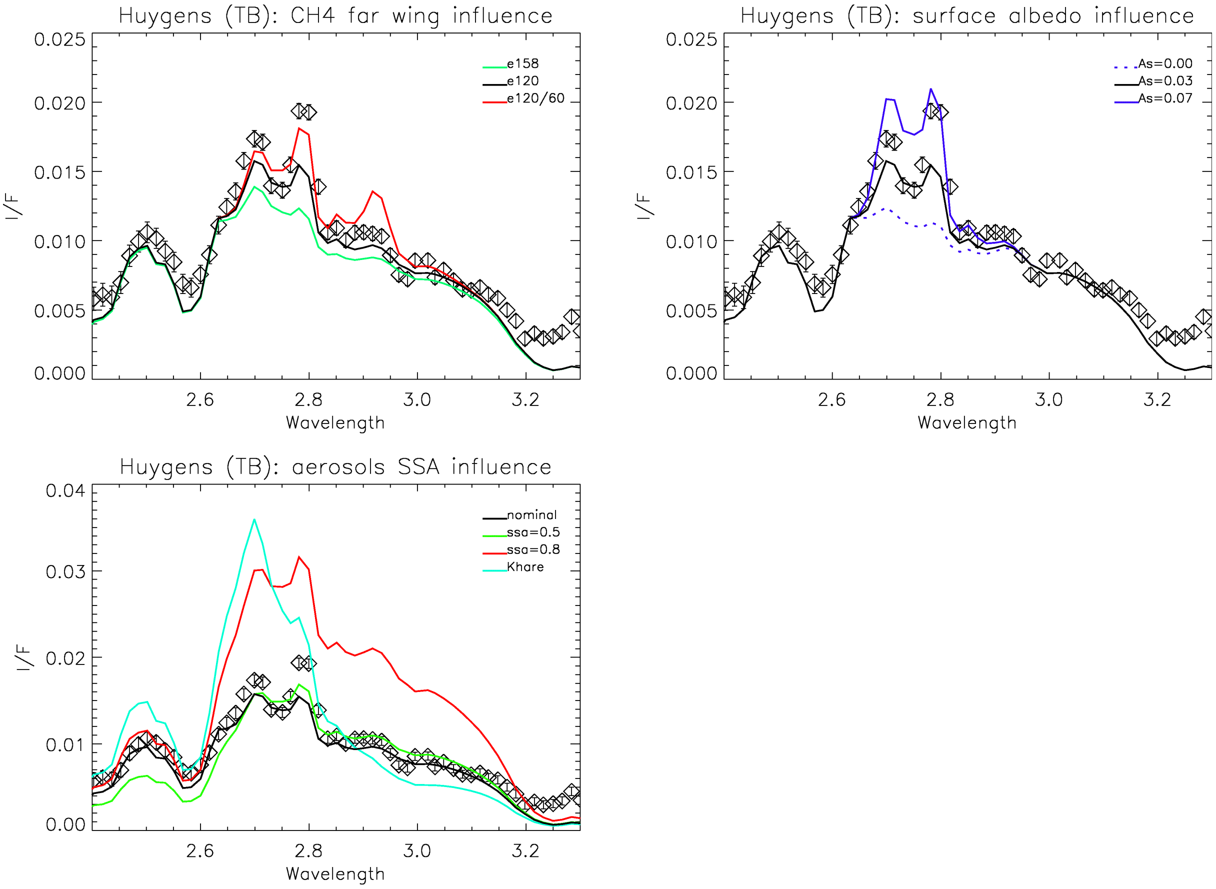

Figure 6. Models of the Huygens landing site spectrum at 2.4 – 3.3 μm. *Top left panel:* effect of far wing line profile, using sub-lorentzian χ factors proportional to *exp*($-\Delta\sigma/120$) (black, nominal case), *exp*($-\Delta\sigma/158$), or composite *exp*($-\Delta\sigma/120$) / *exp*($-\Delta\sigma/60$) (red, see text for details). *Top right panel*: effect of surface albedo: 0.00 (dotted blue), 0.03 (black, nominal case), and 0.07 (solid blue). *Bottom panel*: effect of aerosol single scattering albedo spectrum. Red: ω_0 = 0.80. Green: ω_0 = 0.50 (green). Black: nominal ω_0 spectrum (red line in Fig. 3). Light blue: ω_0 spectrum computed from Khare et al. (1984) indices modified by Rannou et al. (2010) (purple line in Fig. 3).

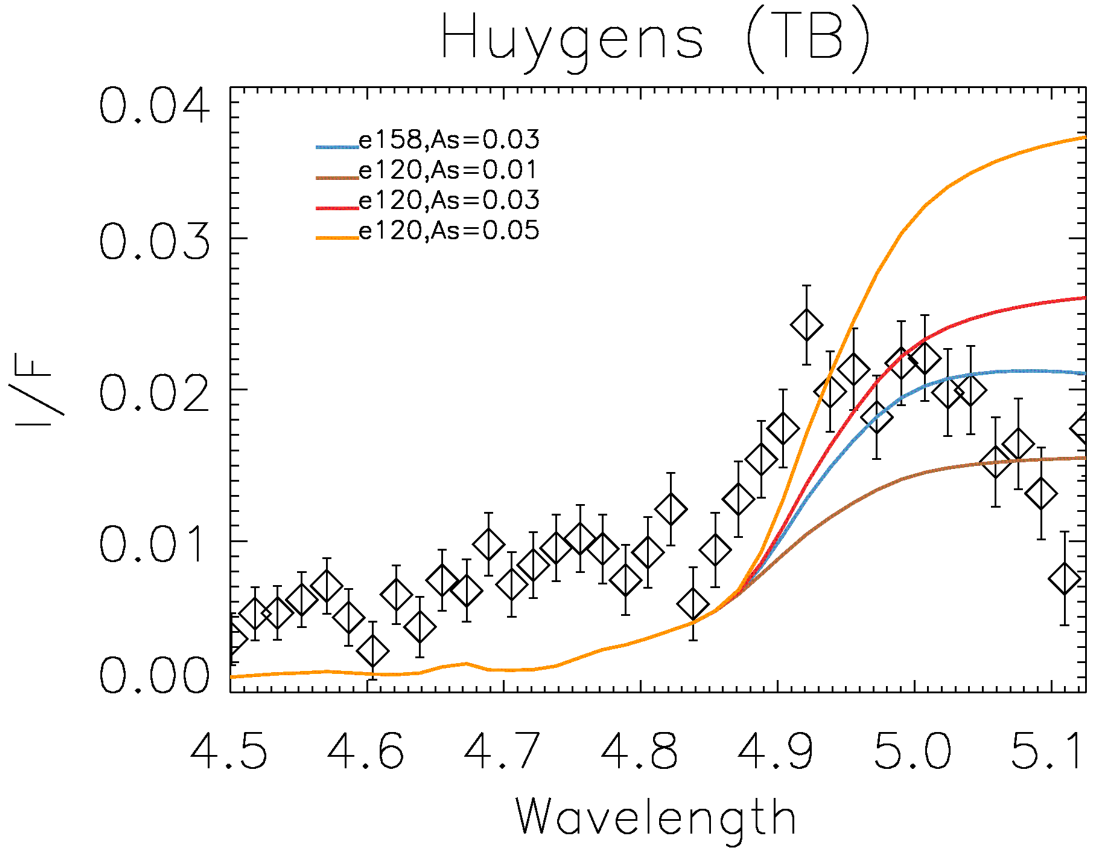

Figure 7. Models of the Huygens landing site spectrum at 4.5 – 5.1 μm as a function of far wing profiles and surface albedo. Orange, red, and brown curves make use of sub-lorentzian χ factors proportional to $exp(-\Delta\sigma/120)$ beyond 26 cm^{-1} of line center, and surface albedos A_s = 0.05, 0.03 and 0.01, respectively. The blue curve has A_S = 0.03 but a χ factor proportional to $exp(-\Delta\sigma/158)$ beyond 26 cm^{-1} of line center. Models include absorption by CO but not fluorescent emission from CO. See text.

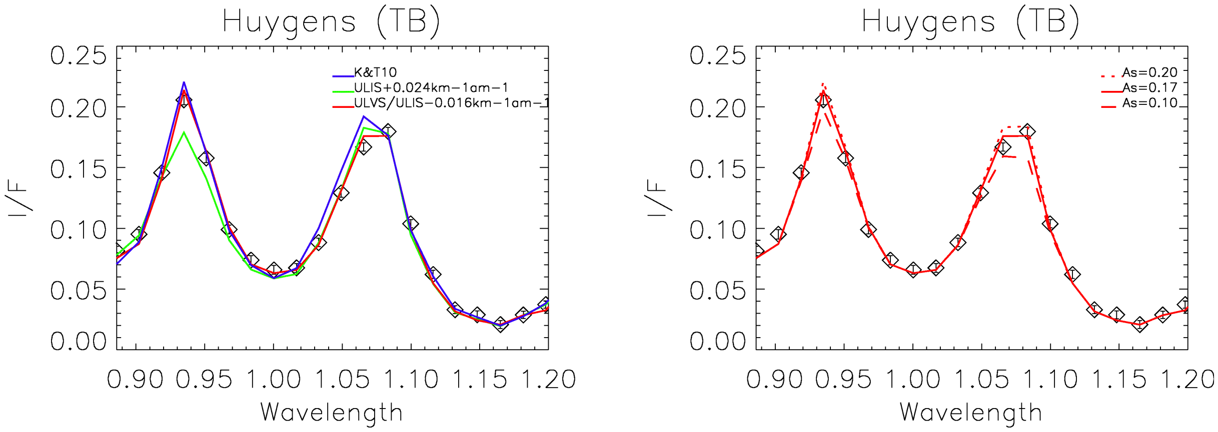

Figure 8. Models of the Huygens landing site spectrum at 0.9 – 1.2 μm. *Left panel:* effect of different treatments of the methane opacity. (i) Green curve: methane absorption calculated from ULIS coefficients from Tomasko et al. (2008a) shifted by +0.024 km^{-1} amagat^{-1} at all wavelengths (ii) Red curve: methane absorption calculated from composite ULVS/ULIS coefficients from Karkoschka and Tomasko (2010), corrected by -0.016 km^{-1} amagat^{-1} longward of 1 μm (iii) Blue curve: methane absorption calculated with the band model from Karkoschka and Tomasko (2010). All calculations were done using a surface albedo of 0.17. *Right panel*: effect of surface albedo, using the corrected ULVS/ULIS methane coefficients: A_s= 0.10 (dashed line), 0.17 (solid line), and 0.20 (dotted line). See text for further explanations.

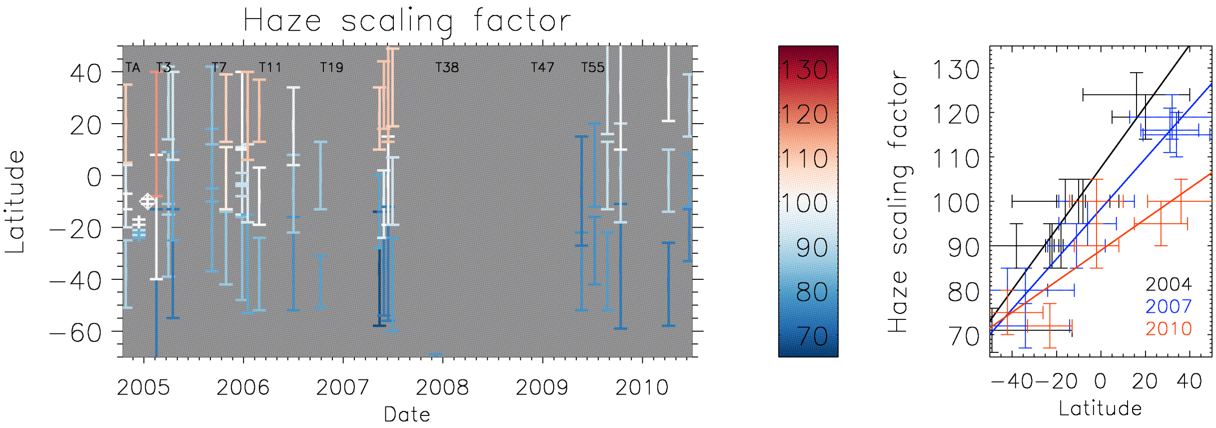

Figure 9. Temporal and latitudinal variation of haze content, expressed as a scaling factor (F) with respect to DISR-measured haze opacity. *Left panel:* haze variations for the "South", "Equator" and "North" regions, observed from late 2004-early 2005 to mid-2010. Color scale varies from 70 % to 130 % of the DISR haze optical depth as indicated in the color bar. The white diamond marks the DISR reference. *Right panel.* Latitudinal profiles at three epochs: Black: 2004 (TA, TB, and T3); Blue: 2007 (T30, T31, and T32); Red; 2010 (T67 and T70). The solid lines indicate linear fitting for the three sets.

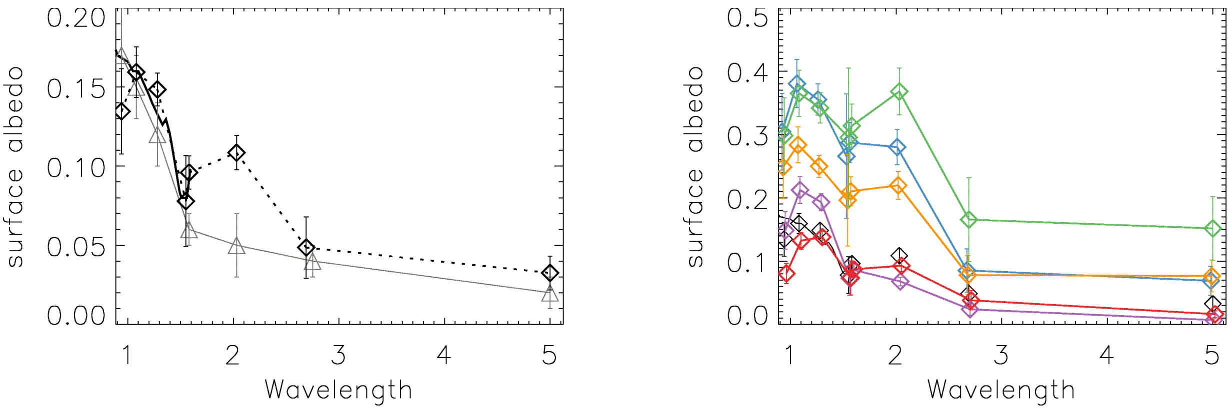

Figure 10. Surface albedos for each methane window: *Left panel:* Albedos at the Huygens landing side (HLS) retrieved from this work (black diamonds), compared to Jacquemart et al. (2008) (black curve) and Griffith et al. (2012) (gray triangles). *Right panel:* Surface albedos retrieved in this work for the five RoIs, compared to the HLS surface albedo spectrum (black diamonds). “Dark Brown” (red), “Dark Blue” (purple), “Bright Brown” (orange), “Bright Blue” (blue), and “Bright Tui” (green). See text for additional explanations.

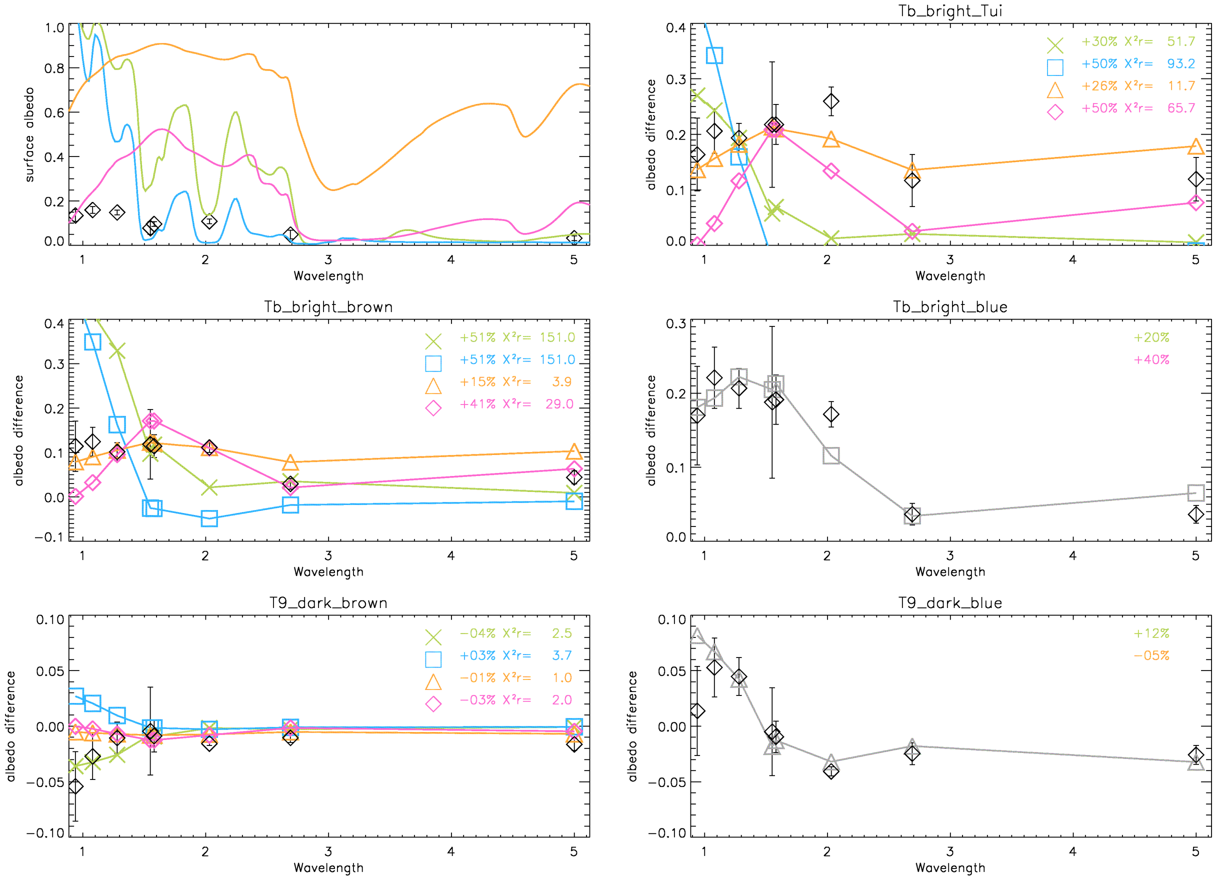
surface albedo
1.0
0.8
0.6
0.4
0.2
0.0
1
2
3
4
5
Wavelength
Tb_bright_Tui
albedo difference
+30% X²r= 51.7
+50% X²r= 93.2
+26% X²r= 11.7
+50% X²r= 65.7
Tb_bright_brown
+51% X²r= 151.0
+51% X²r= 151.0
+15% X²r= 3.9
+41% X²r= 29.0
Tb_bright_blue
+20%
+40%
T9_dark_brown
−04% X²r= 2.5
+03% X²r= 3.7
−01% X²r= 1.0
−03% X²r= 2.0
T9_dark_blue
+12%
−05%
0.10
0.05
0.00
−0.05
−0.10
0.3
0.1
−0.1

Figure 11: Tentative interpretation of surface albedo variability. Upper-left panel: HLS surface albedo spectrum compared to four pure chemical candidates: water ice (100 and 1000 μm grains in green and blue respectively) and tholins (1 and 30 μm grains in orange and pink). In the other panels (one for each of the five RoIs: “Bright Tui”, “Bright Brown”, “Bright Blue”, “Dark Brown”, and “Dark Blue”), the black diamonds indicate the difference between the RoI and the HLS surface spectra, and the difference spectra are fit by adding/subtracting one of the four candidate material spectra at the expense of the HLS surface albedo (see text for details). In each panel, the best fits with water ice (small grains: green crosses; large grains: blue squares) or tholins (small grains: orange triangles; large grains: pink diamonds) are shown separately, with the corresponding reduced χ^2_r indicated. In several cases, the resulting χ^2_r exceed expectations from purely Gaussian noise, pointing to systematic model errors. “Bright Brown”, “Dark Brown” and “Bright Tui” can be reasonably fit by varying one component only. In contrast, “dark blue” and “bright blue” require combinations of surface components. In these cases (bottom two right panels), the best fit is indicated by gray lines and symbols and the “recipe” is indicated. For example, the spectrum of “bright blue” is fit by replacing 60 % of the Huygens albedo by 40 % of 30-μm tholins and 20 % of 100-μm water ice. Similarly, “dark blue” shows an excess of water ice (+12% 100-μm H_2O) and a depletion of 1-μm tholins (-5%).